Bio-Design and Manufacturing (2024) 7:240–261
https://doi.org/10.1007/s42242-024-00281-7

RESEARCH ARTICLE

An oxygenating colloidal bioink for the engineering of biomimetic tissue constructs

Seol-Ha Jeong[1] · Jarno Hiemstra[1,2] · Patrick V. Blokzijl[1,2] · Rebeca Damian-Ferrara[1] · Danilo Martins dos Santos[1,3] · Jéssica H. L. da Fonseca[1] · Min-Ho Kang[4,5] · Jihyun Kim[1] · Dilara Yilmaz-Aykut[1] · Mei L. L. Cham-Pérez[1] · Jeroen Leijten[2] · Su Ryon Shin[1]

Received: 23 December 2023 / Accepted: 2 April 2024 / Published online: 16 May 2024

Abstract

Ensuring a sufficient oxygen supply is pivotal for the success of bioprinting applications since it fosters tissue integration and natural regeneration. Variation in oxygen concentration among diverse tissues necessitates the precise recreation of tissue-specific oxygen levels in imprinted constructs to support the survival of targeted cells. Although oxygen-releasing biomaterials, such as oxygen-generating microparticles (OMPs), have shown promise for enhancing the oxygen supply of microenvironments in injured tissues, whether this approach is scalable for large tissues and whether tissue-specific bioinks with varying OMP concentrations remain printable remain unknown. This study addresses this critical gap by introducing an innovative class of engineered oxygenated bioinks that combine colloidal-based microgels with OMPs. We report that incorporating nanosized calcium peroxide ($nCaO_2$) and manganese oxide nanosheets ($nMnO_2$) into hydrophobic polymeric microparticles enables precise modulation of oxygen release while controlling hydrogen peroxide release. Moreover, the fabrication of oxygenating and cytocompatible colloidal gels is achieved using an aqueous two-phase system. This study thoroughly evaluates the fundamental characteristics of the resulting bioink, including its rheological behaviors, printability, shape fidelity, mechanical properties, and oxygen release properties. Moreover, this study demonstrates the macroscopic scalability and cytocompatibility of printed constructs produced via cell-laden oxygenating colloidal bioinks. By showcasing the effectiveness of extrusion-based bioprinting, this study underscores how it can be used to fabricate biomimetic tissues, indicating its potential for new applications. The findings presented here advance the bioprinting field by achieving scalability with both high cell viability and the possibility of mimicking specifically oxygenated tissues. This work thereby offers a promising avenue for the development of functional tissues with enhanced physiological relevance.

✉ Su Ryon Shin
sshin4@bwh.harvard.edu

1 Division of Engineering in Medicine, Department of Medicine, Brigham and Women's Hospital, Harvard Medical School, Boston, MA 02139, USA

2 Leijten Lab, Department of Developmental BioEngineering, Faculty of Science and Technology, Technical Medical Centre, University of Twente, Drienerlolaan 5, 7522 NB Enschede, The Netherlands

3 Nanotechnology National Laboratory for Agriculture (LNNA), Embrapa Instrumentação, Sao Carlos, Sao Paulo 13560-970, Brazil

4 Department of Biomedical-Chemical Engineering, The Catholic University of Korea, 43 Jibong-ro, Bucheon-si, Gyeonggi-do 14662, Republic of Korea

5 Department of Biotechnology, The Catholic University of Korea, 43 Jibong-ro, Bucheon-si, Gyeonggi-do 14662, Republic of Korea

Graphic abstract

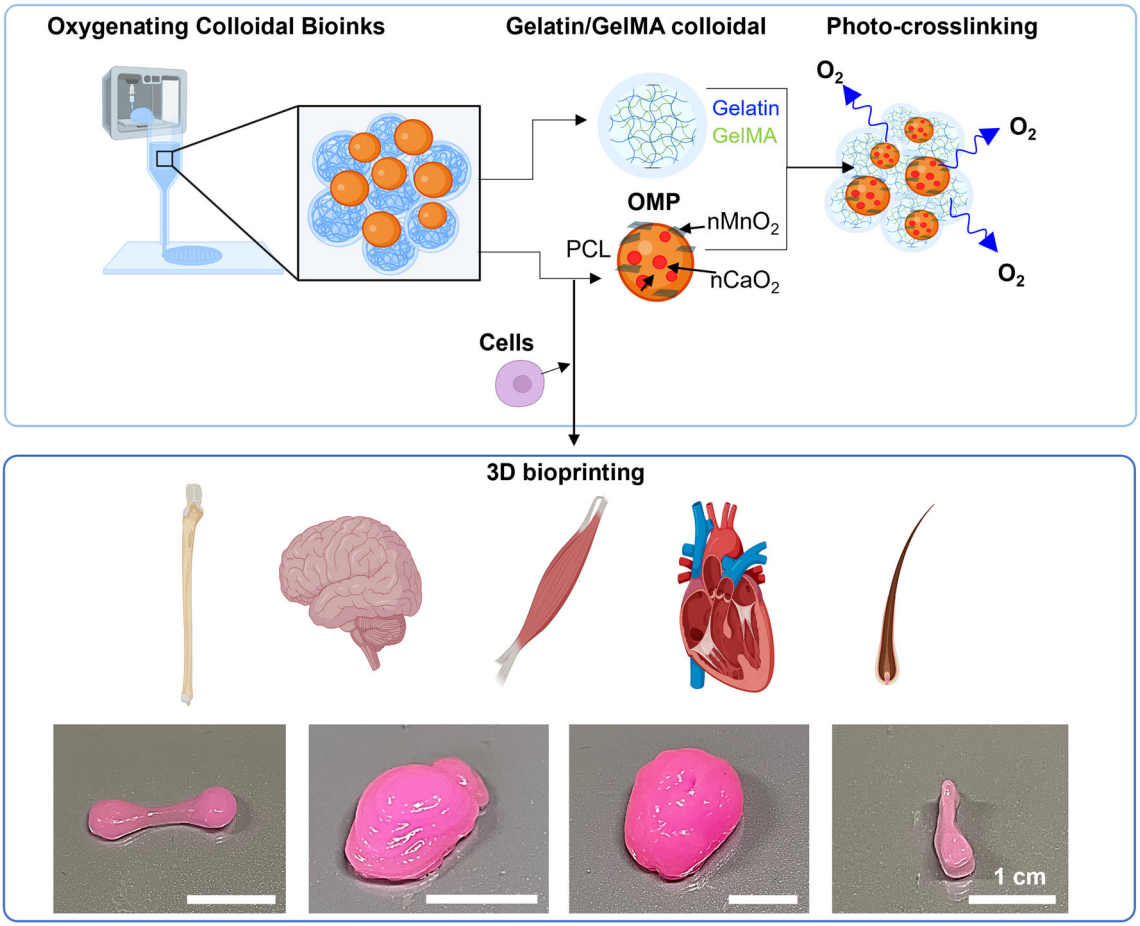

Keywords 3D bioprinting · Bioink · Colloidal gels · Extrusion printing · Oxygen-generating microparticle

Introduction

Three-dimensional (3D) bioprinting is an advanced technology for creating tailored scaffolds capable of mimicking the intricate architecture found in natural tissues [1–3]. It uses the volumetric deposition of biomaterial-based bioinks to facilitate the biofabrication of scalable, structurally complex, and functional 3D tissue constructs that mimic native tissues [4, 5]. Typically, hydrogels are considered highly effective frameworks since they provide excellent microenvironments that both maintain high cell viability and improve cellular behavior by tuning intricate biochemical and biomechanical cues and mimicking native extracellular matrixes (ECMs) [6, 7]. However, one challenge associated with both conventional and large-scale bulk hydrogels is that pores within the polymeric matrix can restrict cell mobility and hinder the diffusion of oxygen and nutrients from outside, thereby limiting cell viability and infiltration [8]. Ensuring the survival of transplanted cells in engineered 3D tissue constructs at the early stages—i.e., before the regeneration of new blood vessels—presents a significant challenge for practical applications involving engineered tissues [9]. Thus, a microstructural design that possesses high interconnectivity among bioprinted hydrogel-based constructs is required to promote tissue integrity following printing for clinical applications [10].

Microgels are outstanding bioink components for bioprinting systems due to their porous microstructures [11–17]. Although many approaches are used to fabricate microgels, among the most reliable are aqueous two-phase systems, which contain two different aqueous polymers [18–20]. Since these systems require no surfactants, particulate stabilizers, or organic solvents to induce phase-separated microsized droplets, they eliminate the need for additional remnant reagent removal steps. This makes the bioink preparation

more accessible and helps it to achieve high biocompatibility, thereby enabling cell encapsulation within the bioink [21]. Overall, many bioink combinations—involving both cells and microgels—can be employed to engineer 3D tissue constructs, which in turn offer a potential treatment for volumetric tissue defects [22–24].

To achieve successful clinical application, in which biofabricated constructs are seamlessly integrated into the host's surrounding tissues and undergo natural regeneration, it is imperative to ensure that constructs receive an oxygen supply capable of maintaining the required oxygen level for a specific tissue region. Specificity is required because cells targeted for regeneration within a given tissue are extruded and deposited into the injured area, and the oxygen concentrations of various tissues within the human body are subject to tight biological regulation. Overall, oxygen levels are known to play a crucial role in numerous physiological processes [25, 26]. Therefore, it is essential to create constructs with varying oxygen concentrations to foster the development of well-oxygenated tissues. In particular, oxygen-releasing biomaterials can promote the viability of living implants by ensuring that the oxygen levels provided are adequate to support biomaterial survival [27–29]. Extensive research has been conducted in the field of oxygen generation, but many studies have focused on chemical reactions involving peroxide materials, which produce oxygen when exposed to water [27, 30–32]. The use of oxygen-generating microparticles (OMPs) has facilitated improvement in the oxygen supply within various injured tissue microenvironments, including critical bone defects [33–35], volumetric muscle loss [28], cartilage defects [36], myocardial infarcted regions [37], and severe wounds [38–40]. However, the scalability and printability of tissue-specific bioinks with different OMP concentrations for fabricating engineered 3D tissue constructs, along with their oxygen release properties, have not yet been fully examined.

The materials that release oxygen can be classified into two primary types: O_2 carriers and O_2 generators [41]. O_2 carriers, including cyclodextrin [42] and perfluorocarbons [43], are artificial materials designed to mimic erythrocytes. In contrast, O_2 generators use peroxides such as calcium peroxide (CaO_2) or algae to release new oxygen. Notably, algae have recently gained attention due to their natural, environmentally friendly, cost-effective, and sustainable oxygen-producing capabilities [44]. However, the reliance of photosynthetic algae on light for oxygen production limits their suitability as synthetic erythrocytes, since blood is predominantly found deep within the body, where photosynthesis is not possible.

Since the intermediate generation of H_2O_2 is unavoidable, various approaches to manipulate H_2O_2 release by incorporating catalase or catalase-like materials have also been introduced [45]. Catalase, which specifically catalyzes the breakdown of H_2O_2 into water and oxygen, has been widely employed to reduce H_2O_2 levels in solid peroxide materials [46]. However, its effectiveness is hindered by its extremely short half-life under physiological conditions, which makes it unsustainable for prolonged implantation periods. Moreover, catalase is prone to denaturation during processing and application, thereby limiting its applicability. An alternative approach involves incorporating catalase onto the surface of OMPs using a polymeric coating layer composed of gelatin. However, this method faces challenges related to the stability of catalase during microfabrication, since both gelatin and gelatin methacryloyl (GelMA) require temperatures for dissolution that are high enough to negatively impact catalase activity. However, catalase-like materials such as MnO_2 nanostructures demonstrate remarkable catalase-like activity and enhanced stability [47]. Nanomaterials based on MnO_2 (also known as "nanozymes") can convert endogenous H_2O_2 to O_2, thereby mitigating tissue hypoxia.

In this study, we introduce an innovative category of engineered oxygenated bioinks involving a combination of colloidal-based microgels and OMPs. To modulate oxygen release while controlling hydrogen peroxide (H_2O_2) release, nanosized calcium peroxide ($nCaO_2$) and MnO_2 nanosheets ($nMnO_2$) were immobilized within hydrophobic polymeric microparticles [48]. A significant advantage of incorporating both components into a hydrophobic polymeric matrix is that the resulting material can create sustained oxygen release systems and effectively convert H_2O_2 to O_2. In addition, this approach avoids the accumulation of cytotoxic levels of H_2O_2, which typically limits the use of peroxides as oxygen sources for biomaterials. Next, we performed an evaluation of the fundamental characteristics of the bioinks, including their rheological behaviors, printability, shape fidelity, mechanical properties, and oxygen release behaviors. We conclude with a comprehensive assessment of printed constructs for macroscopic scalability and cytocompatibility using 3D cell encapsulation.

Materials and methods

Materials

Gelatin from porcine skin (type A), poly(ethylene oxide) (PEO, average molecular weight of 300,000 g/mol), poly(ethylene glycol) (PEG, average molecular weight of 400 g/mol), polycaprolactone (PCL, average molecular weight of 45,000 g/mol), sodium chloride (NaCl),

sodium hydroxide (NaOH), ethyl acetate, calcium chloride ($CaCl_2$), potassium permanganate ($KMnO_4$), methacrylic anhydride (MA), isopropanol (IPA), 2-hydroxy-4-(2-hydroxyethoxy)-2-methylpropiophenone (Irgacure 2959), hydrogen peroxide, ammonium hydroxide, dimethylsulfoxide (DMSO), dichloromethane (DCM), Pluronic F-127, *o*-phthaldialdehyde reagent (OPA), fluorescein isothiocyanate (FITC), fluorescein isothiocyanate-dextran (FITC-dextran, 2000 kDa), rhodamine, ethyl alcohol, and collagenase type IV were all purchased from Sigma-Aldrich (USA). All materials were used as received unless otherwise reported. Dulbecco's phosphate-buffered saline (1×) and distilled water (DI) were purchased from Gibco (USA). Finally, a Sylgard 184 Silicone Elastomer Kit was purchased from Dow Corning (USA).

Methods

Synthesis of gelatin methacryloyl (GelMA)

GelMA was synthesized following a previously established protocol [49]. In summary, a 10% (0.1 g/mL) gelatin solution was prepared in sterile phosphate-buffered saline (PBS) under continuous stirring at 50 °C at a rotation speed of 240 r/min. This continued for 30 min until a uniform consistency was achieved. Throughout this process, the agitation and temperature conditions were maintained, and 0.5 mL of MA was gradually added. Continuous stirring at 50 °C was sustained for 2 h, after which the reaction was stopped by adding 200 mL of prewarmed PBS. Subsequently, the reaction solution was then dialyzed in DI for five days using dialysis membranes. This procedure used a molecular weight cutoff of 12–14 kDa to eliminate any unreacted MA. Finally, the solution was filtered through a 0.22-μm-pore size filtration cup before being subjected to a five-day lyophilization process. The degree of methacrylation (DoM) was then assessed using OPA [23]. In brief, GelMA was dissolved in PBS at 0.5 mg/mL before being mixed at a 1:1 volume ratio with OPA. Subsequently, 200 μL of each of these solutions was added to separate wells in a 96-well plate, with each condition repeated in triplicate. Fluorescence intensity was measured using a microplate reader set at excitation and emission wavelengths of 340 and 455 nm, respectively. The DoM was subsequently determined using the following formula:

$$\mathrm{DoM} = \frac{I_{\mathrm{sample}} - I_{\mathrm{blank}}}{I_{\mathrm{standard}} - I_{\mathrm{blank}}},$$

where I_{sample} represents the relative intensity of the sample, I_{blank} represents the relative intensity of the blank, and I_{standard} represents the relative intensity of the standard.

Synthesis of $nCaO_2$

Here, $nCaO_2$ was synthesized using a modified precipitation method [48]. Briefly, 3 mL of 0.9 mol/L $CaCl_2{\cdot}2H_2O$ aqueous solution was mixed with 12 mL of a 0.01 g/mL aqueous solution of PEG under magnetic stirring at room temperature. Next, 100 μL of ammonium hydroxide solution was added to the medium, and 1.5 mL of 30% hydrogen peroxide was slowly added at 0.2 mL/min as the reaction medium was stirred for 2 h at room temperature. Finally, 0.1 mol/L NaOH aqueous solution was added to adjust the pH to 11.5. The resulting suspension was then centrifuged at 8000 r/min for 10 min, after which the resulting white precipitate was sequentially washed with 0.1 mol/L NaOH, DI, and absolute ethanol. Finally, $nCaO_2$s were then dried at 80 °C for 2 h before being stored in a desiccator.

Synthesis of $nMnO_2$

$nMnO_2$ was prepared following the method reported by Sinha et al. [50] and dos Santos et al. [48] with some minor adjustments. Briefly, a round-bottomed flask was used to combine 150 mL of a 20 mmol/L $KMnO_4$ aqueous solution with 40 mL of ethyl acetate, resulting in a biphasic mixture. This mixture was then subjected to reflux at 85 °C in an oil bath for 16 h. The resulting colloidal suspension of $nMnO_2$ nanosheets was transferred to a separating funnel to eliminate ethyl acetate. Next, the precipitate was meticulously washed, first with deionized water and later with absolute ethanol. Afterward, $nMnO_2$ was dried at 50 °C for 4 h and preserved in a desiccator until further use and characterization.

Fabrication of OMPs

OMPs were prepared using the cosolvent precipitation method [34]. Briefly, 500 mg of PCL (average molecular weight of 45,000 g/mol) was dissolved in 10 mL of DCM, after which 50 mg $nCaO_2$ and 5 mg $nMnO_2$ were suspended in the polymeric solution using tip ultrasonication for 4 min. Next, 2 mL of the resulting suspension was added dropwise to 4 mL of 25 mg/mL Pluronic 127 solution. This was vortexed for 1 min and then dispersed by tip ultrasonication for 5 min, resulting in OMP dispersion. Microparticles were subsequently added to a 5 mg/mL aqueous solution of Pluronic 127 and stirred in a fume hood for an additional 2.5 h at 60 °C; this allowed DCM evaporation and was followed by centrifugation at 5000 r/min for 1 min. The resulting microspheres were then further centrifuged at 5000 r/min for 1 min, washed with DI three times, frozen at −80 °C, freeze-dried at −45 °C for 48 h, and then stored at 25 °C for further use and characterization. In this study, most OMPs were synthesized following the procedure described above and were used as

controls. However, to characterize differing OMP morphologies, rhodamine-conjugated PCL was synthesized according to the literature [51], and OMP was also fabricated using this compound. The resulting particles were observed using a confocal laser scanning microscope (CLSM, Leica SP8X STED Microscope, Germany).

Fabrication of colloidal hydrogels

To prepare colloidal gels, 125 mg gelatin and 125 mg GelMA with approximately 30% DoM were first dissolved in 2.5 mL DI. In addition, 90 mg NaCl was dissolved in 2 mL DI. All three mixtures were placed in a water bath at 50 °C for 25 min, after which they were mixed by vortexing for 30 s before being returned to the water bath at 50 °C for another 5 min. Once dissolved, the mixture was added to the PEO solution and vortexed until a thick, opaque consistency was observed. The resulting mixture was then left on ice for 20 min. Subsequently, this mixture was centrifuged at 4 °C at a speed under 4000 r/min for 20 min, after which the supernatant was removed. Next, we added 10% (volume fraction) $CaCl_2$ solution (1 mol/L) and DI (i.e., in a 1:1 volume ratio). These solutions were vortexed for 30 s and centrifuged at 4 °C under 4000 r/min for 20 min. Finally, the supernatant was removed from solution and stored at 4 °C until further use.

Fabrication of OMP-laden colloidal hydrogels (OMP-Gel)

To fabricate OMP-laden hydrogels, we first used 1 mL 2% GelMA with a high DoM (i.e., approximately 60%) to disperse different concentrations of OMPs. The volume of OMP added varied depending on the desired concentration (i.e., 0, 5, 10, or 25 mg in 5 mL of DI). To obtain a fully homogenized mixture, tip ultrasonication was performed for 5 min. The suspension was then centrifuged for 5 min at 4000 r/min at room temperature to remove residual GelMA solution. After 1 mL of DI was added, the OMP suspension was again sonicated under the same conditions for 5 min using an ice bath. Subsequently, the OMP solution was added to the 5 mL of colloidal gels and gently mixed. After centrifuging to remove the remaining DI, 0.25% Irgacure 2959 was dissolved in 750 μL of DI and was mixed. Thereafter, the resulting solution was centrifuged for 5 min at 4000 r/min at 4 °C after which the supernatant was removed. Finally, the bioink was transferred into a 5-mL syringe for printing. After printing, it was exposed to ultraviolet (UV) light at 800 mW/cm^2 for 30 s to crosslink the bioink. To characterize OMP-Gel morphology, we examined FITC-conjugated GelMA using a confocal microscope [52] (CLSM, Leica SP8X STED Microscope, Germany).

Dynamic light scattering (DLS)

The sizes of OMPs and colloidal hydrogels were determined by DLS using a Zetasizer Nano ZS equipped with a He–Ne laser (λ=633 nm) at a scattering angle of 137° (Malvern Instruments, UK).

Scanning electron microscopy (SEM)

We characterized the surface morphology of OMPs and the cross-sectional microstructure of OMP-Gel using a field emission scanning electron microscope (FE-SEM, Zeiss Gemini 560 FE-SEM, Germany) under an accelerating voltage of 15 kV. Before loading, all freeze-dried samples were coated with a Pt/Pd 80/20 alloy using an EMS 150 T S Metal Sputter Coater (Electron Microscopy Sciences, USA).

Transmission electron microscopy (TEM)

Next, the structure and chemical composition of synthesized $nCaO_2$ and $nMnO_2$ materials were examined using transmission electron microscopy (TEM, JEM-2100F, JEOL, Japan) coupled with energy-dispersive X-ray spectroscopy (EDS) at an accelerating voltage of 200 kV. To disperse nanoparticles homogeneously, we sonicated $nMnO_2$ in DI for 5 min using bath sonication. $nCaO_2$ (10 mg/mL) was dispersed in 1 mL of IPA, followed by 10 min of sonication. Subsequently, a 100 μL drop of sample suspension solution was deposited onto an ultrathin carbon (15–25 nm) film TEM grid. After complete drying of the grid for one day, TEM imaging was performed.

Porosity and particle analyses of pure colloidal gels

Next, we conducted porosity and particle size analyses of all generated materials. To do so, crosslinked colloidal hydrogels were first placed in PBS for 24 h to ensure complete removal of gelatin microparticles. Subsequently, colloidal hydrogel samples were incubated in PBS containing 1 mg/mL of 2000 kDa of FITC-dextran at 37 °C for 24 h. The colloidal hydrogels were then imaged using a CLSM (Leica SP8X STED Microscope, Germany). Finally, porosity and particle size analyses were performed using MATLAB on individual images taken from the z-stack. Void space was gathered using the porosity analysis results.

Hydrolytic stability tests

Four different colloidal bioinks with different OMP concentrations (i.e., 0.0% (0 g/mL), 0.1% (0.001 g/mL), 0.2% (0.002 g/mL), and 0.5% (0.005 g/mL)) were used. For each sample, approximately 700 μL of each bioink was set into a predesigned cylindrical polydimethylsiloxane (PDMS) mold

to yield cylindrical designs with a diameter of 4.48 mm and a height of 4.50 mm. Afterward, these were then crosslinked using UV light exposure at 800 mW/cm^2 for 30 s. The resulting colloidal hydrogels were placed in 1 mL of PBS, and after 24 h, the wet weight was measured every 2 h for the first 12 h and at 24-h intervals for the following seven days. PBS was refreshed every 48 h.

$$\text{Relative mass} = \frac{W_{\text{measured}}}{W_{\text{initial}}},$$

where W_{measured} represents the weight of the sample measured after certain time interval and W_{initial} represents the initial weight of the sample.

Enzymatic degradation tests

We then analyzed enzymatic degradation. To do so, colloidal hydrogels were first prepared in a manner similar to that used for the hydrolytic stability test. The resulting colloidal gels were placed in PBS with 1.5 μg/mL collagenase type IV (255 U/mg) at 37 °C and over a period of 12 days, and the mass of the colloidal hydrogels was measured at specific time points over seven days. Another sample of OMP-laden colloidal hydrogels was placed in PBS with 2 μg/mL collagenase type IV at 37 °C, and the mass of the colloidal hydrogel was also measured at specific time points. The PBS with collagenase solution was changed every 48 h to ensure that the enzyme remained active. Degradation was evaluated by determining mass loss over time.

$$\text{Relative mass} = \frac{W'_{\text{measured}}}{W'_{\text{initial}}},$$

where W'_{measured} represents the weight of the sample measured after degradation in certain time interval and W'_{initial} represents the initial weight of the sample.

Compression tests

Compression tests were performed using a 3342 Single column universal material testing system (Instron, USA). Colloidal hydrogel disks with a height of 5 mm and a diameter of 5 mm were prepared for each gel type and were incubated at 37 °C for 24 h to ensure gelatin leaching. Before each measurement, the exact height and diameter of each gel were determined, after which compression tests were performed. For each sample, the Young's modulus was calculated by determining the slope of the linear region of the curve (5%–15% strain) using MATLAB.

Rheological tests

Next, we performed viscosity assessments of OMP-laden colloidal bioinks using a rheometer (HR-3, TA Instruments, USA). For this analysis, 200 μL of each bioink was loaded onto the rheometer's flat plate (20 mm diameter). Viscosity measurements were performed within a shear rate range of 0.01–100 s^{-1} and as a function of frequency within the range of 0.1–100 Hz, all at a 0.1% strain and a temperature of 4 °C. The recovery behavior of the bioink was evaluated using a step-strain sweep approach, where a low strain (1%) and a high strain (90%) were cyclically applied every 100 s at a frequency of 1 Hz, as per a previously established method [53].

Printability and shape fidelity tests

For printability evaluation, two layers of bioinks containing different OMP concentrations (i.e., 0.0%, 0.1%, 0.2%, and 0.5%) were deposited following a 0°–90° pattern with increasing distances between filaments [3]. The inter-filament distance ranged from 1 to 5 mm and increased by 1 mm on each step. In addition, we used three needle tips (i.e., 22G, 25G, and 30G) to assess printing resolution at different needle outlet diameters. Images were taken immediately after printing to avoid drying. Subsequently, images of all printed shapes were measured using NIH ImageJ. The printability index (P_{r}) was calculated using the following equation:

$$P_{\text{r}} = \frac{L^2}{16A},$$

where L represents the pore perimeter and A denotes the area. A printability index of 1.0 indicates a perfectly square pore and suggests that the printed structure closely matches the intended design.

Oxygen measurement

Next, we performed oxygen measurements on 500 μL OMP-laden colloidal gels. To do so, gels were first prepared in the microtubes and placed in an anoxic (i.e., O_2 level 0.1%) chamber (BioSpherix ProOX21 with C-chamber) overnight with the addition of 500 μL of nitrogen gas (N_2) to purge PBS. Subsequently, an optical sensor probe (Opto-F1 Uni-Amp optode, Unisense, USA) was added to each of the gels to measure oxygen release. Next, to quantify hydrogel oxygen influx, disk-shaped hydrogels with a height of 5 mm and a diameter of 5 mm were prepared for both colloidal and bulk GelMA hydrogels. These were placed in an anoxic (O_2 level 0.1%) chamber (BioSpherix ProOX21 with C-chamber) overnight and an optic sensor probe was used to measure real-time oxygen levels. After the measured oxygen levels within

the anoxic chamber stabilized, the probe was transferred into the colloidal gel samples and oxygen was allowed in by opening the anoxic chamber. All data were further processed using MATLAB.

Cytotoxicity tests of OMPs

For cytotoxicity testing, human dermal fibroblasts (HDFs, ATCC, USA) with a density of 5×10^4 mL^{-1} were seeded in 96-well plates until full confluency was reached. After replacing with a culture medium containing various concentrations of OMPs, all cells were cultured under both normoxic and hypoxic (1% oxygen) conditions (n=3) for one day. Finally, a Presto Blue cell viability assay (Invitrogen, USA) was performed to observe cell viability.

In vitro cell encapsulation for bioprinting

Human mesenchymal stem cells (hMSCs, ATCC, USA) and HDFs were first cultured in Dulbecco's modified eagle medium (DMEM, Gibco, USA) supplemented with 10% fetal bovine serum (FBS, Gibco). Culturing proceeded under high or low glucose conditions with 1% penicillin–streptomycin (Gibco, USA) at 37 °C in 5% CO_2 in a humidified incubator. After preparing pure colloidal gel bioinks and 0.1% OMP-Gel bioinks, a cell suspension with a density of 5×10^6 mL^{-1} was gently added to each bioink sample before transferring to a syringe for printing. All post-crosslinking printed constructs were then cultured in a hypoxic chamber (i.e., O_2 level 1%) for seven days. Cells within colloidal hydrogel constructs were stained using a live/dead assay kit (Thermo Scientific, USA) for 30 min; subsequently, we observed the morphology and viability of cells using a fluorescence microscope.

Quantitative real-time polymerase chain reaction (qRT-PCR)

For qRT-PCR, total RNA was first isolated from all samples using TRIzol. Complementary DNA (cDNA) fragments were then synthesized from extracted RNA using a SuperScript III First-Strand Synthesis SuperMix (Invitrogen). Next, we designed primers targeting genes encoding hypoxia-inducible factor-1α (HIF-1α), which were then synthesized by Integrated DNA Technologies, Inc. (Coralville, IA, USA). An advanced Universal SYBR Green SuperMix (Bio-Rad) was used to quantify amplified DNA, and gene expression levels were determined by qRT-PCR using an iQ5 thermocycler (Bio-Rad, USA). Relative gene expression was then assessed using the $2^{-\Delta\Delta C_t}$ method, and all experiments were conducted in triplicate.

Statistical analyses

All statistical analyses were conducted using GraphPad Prism 9 software (GraphPad Software Inc., USA). Reported values represent the mean±standard deviation of three or more independent experiments. The statistical significance of differences in mean and variance was assessed using one-way analysis of variance (ANOVA). Significance levels were denoted as follows: $^{*}p<0.05$, $^{**}p<0.01$, $^{***}p<0.001$, $^{****}p<0.0001$ indicating statistical significance. Finally, we examined the normality of the distributions of void space and particle size of the colloidal gels using Shapiro–Wilk tests.

Results and discussion

Characterization of colloidal gels with various gelatin, GelMA, and PEO ratios

Microporous hydrogels or granular gels have been employed as a supporting bath during the printing process, since they have a relatively high porosity [54, 55]. However, when aiming to 3D-printed bulk constructs designed to mimic specific tissues, material properties that allow for a certain degree of stacking while maintaining structural integrity are required. Hence, we concluded that diminishing the microscale to a few micrometers would enable the creation of a more stable gel structure without adversely affecting nutrient transport and/or cell migration. Thus, an OMP-laden colloidal bioink for printing was prepared as shown in Scheme 1. In brief, colloidal hydrogels and OMPs were prepared separately and then gently mixed together. After removal of the solvent using centrifugation, the photoinitiator and appropriate cells were mixed before printing. For colloidal hydrogel formation, a water-in-water emulsion technique was employed using a GelMA/gelatin mixture and PEO [18]. In this study, we used vortexing to vigorously break down small phase-separated droplets to form higher-resolution colloidal hydrogels. This procedure follows the overview in Scheme 1a and Fig. S1 (Supplementary Information). During colloidal gel preparation, the deionized water-based phase separation between GelMA/gelatin and PEO can be understood from a thermodynamic perspective since it is primarily driven by differences in hydrophilicity between these polymers [18]. Gelatin possesses abundant hydrophilic groups that create strong hydrogen bonds with water molecules, making it well suited for aqueous conditions. In contrast, GelMA is a derivative of gelatin that is slightly hydrophobic due to the presence of methacrylic groups that ordinary gelatin does not possess. However, despite this difference, GelMA still contains hydrophilic groups that serve a similar purpose, but may

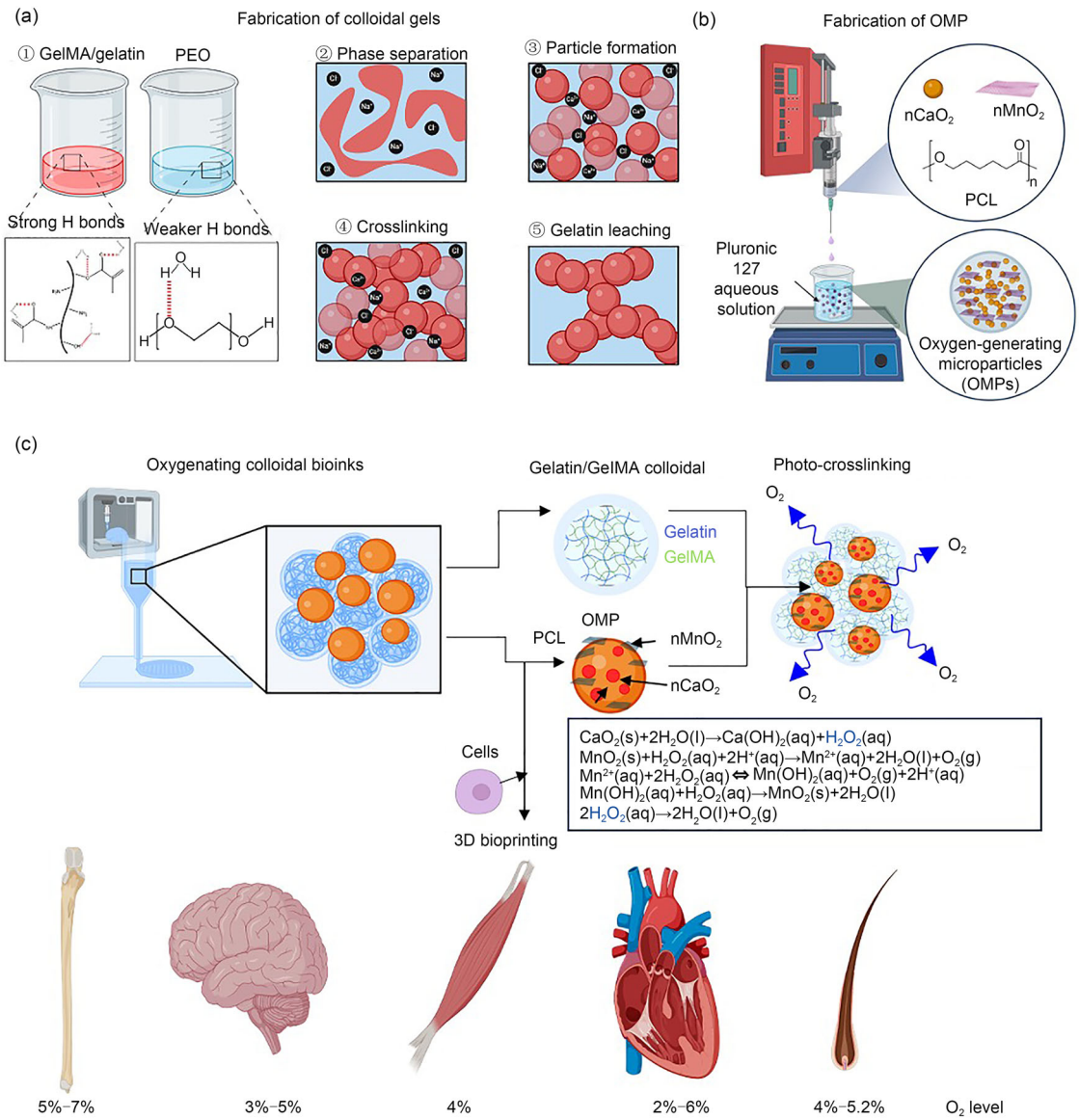

Scheme 1 Schematic illustration of the fabrication of colloidal gels, OMPs, and oxygen-generating colloidal bioinks and their potential applications for tissue construct fabrication. **a** The phase separation of PEO and GelMA involves minimizing the free energy in the system to achieve greater stability. This occurs due to the contrasting hydrophilicity of the two immiscible polymers. PEO shares a structure similar to that of PEG, and its hydrophilicity decreases as its molecular weight increases, making PEO less hydrophilic than GelMA. Consequently, GelMA exhibits stronger interactions with water (via hydrogen bonding) than PEO does with water, or than GelMA and PEO do with each other. This immiscibility arises because mixing is not energetically favorable. To reduce interfacial tension—and the overall free energy of the system—in an energetically favorable manner, GelMA forms particles upon phase separation with PEO. In addition, the introduction of ions (i.e., as NaCl and $CaCl_2$) augments phase separation and enhances particle stability. **b** Fabrication of OMPs by emulsion. **c** For polymers, we chose a gelatin and GelMA mixture based on a colloidal gel with an about 2–3 μm size distribution of colloidal units, since this yields both high porosity and mechanical stability. For OMPs, $nCaO_2$ was selected as an oxygen generator and $nMnO_2$ plays a role as a catalase-like nanozyme. Based on the oxygen levels of the targeted tissue, specified cells can be selected and OMP content can then be modulated to reach the oxygen levels required for specific tissues. OMPs: oxygen-generating microparticles; PEO: poly(ethylene oxide); GelMA: gelatin methacryloyl; PEG: poly(ethylene glycol); PCL: polycaprolactone

participate in specific interactions with PEO [56, 57]. Moreover, although inherently hydrophilic, PEO exhibits reduced hydrophilicity as its molecular weight increases.

To choose the optimal colloidal gels for our composite bioinks, we conducted thorough observations of colloidal gels with different ratios and concentrations of gelatin and GelMA. We first studied the GelMA and gelatin ratio and quantified how it can affect colloidal formation and the overall physical properties of colloidal gels. In Fig. 1a, we present 3D reconstructions of individual *z*-stacks of colloidal hydrogels composed of various ratios of GelMA and gelatin, along with a representative two-dimensional (2D) image. These results showed that most pores were about 2 μm in diameter, which is even smaller than previous reports in the literature [19]. Interestingly, a higher proportion of gelatin in the mix corresponded to a greater relative frequency of smaller pores (Fig. 1b). In addition, higher gelatin ratios yielded smaller particles (Fig. 1c) as well as a larger void space (Fig. 1d) within the hydrogel. This outcome is expected since a higher gelatin ratio results in less crosslinked material within the colloidal hydrogel and fewer particles after the gelatin leaching process. These factors lead to a reduction in particle size and a corresponding increase in void space. In addition, the disparity in hydrophilicity between gelatin and GelMA, caused by the presence of methacrylate groups, may be a significant cause of the formation of smaller colloidal sizes. In addition, the reduction in the amount of crosslinked GelMA material and the presence of larger pores led us to predict that these materials would have a reduced Young's modulus, as demonstrated in Fig. 1e. Interestingly, the 100/0 GelMA/gelatin colloidal gels exhibited lower Young's modulus values than 75/25 GelMA/gelatin colloidal gels. Figure 1f and Fig. S2 (Supplementary Information) illustrate the weight-to-weight and volume-to-volume swelling of the gels over time. Remarkably, within a 24-h timeframe, a noticeable decline in both weight and volume was evident, primarily due to the leaching of gelatin from the hydrogel, thereby indicating initial hydrolytic degradation. Following gelatin dissolution, all colloidal hydrogels exhibited consistent relative mass over time. Thus, relative mass was closely correlated with gelatin content, since a higher gelatin content resulted in a lower ratio of sample measured weight.

We also found that all colloidal gels displayed sustainable hydrolytic stability for seven days. However, when exposed to enzymatic solutions containing type IV collagenase to replicate physiological conditions, the degradation rate increased with a higher proportion of gelatin (Fig. 1g). The deviation in mass loss from the gelatin content, particularly for the 100/0 and 75/25 GelMA:gelatin samples, can be attributed primarily to the impact of enzymatic degradation on the collagen crosslinking networks within the colloidal gel matrix. This is why the 75/25 ratio exhibited a comparatively slower degradation relative to the other groups. Despite lower GelMA content, the increased crosslinking networks among colloidal particles contributed to a slightly slower degradation than for the 100/0 ratio, a trend that is consistent with observed mechanical properties (Fig. 1e). Since PEO can also generate voids, which also affect the physical and mechanical properties of colloidal gels, different ratios of polymers, including gelatin and GelMA, to PEO were also prepared. We then observed similar outcomes when the polymer:PEO ratio was varied during colloidal hydrogel fabrication (Fig. 2). Specifically, we found that an increase in the PEO ratio yielded results comparable to an increased gelatin ratio (Figs. 2a and 2b). This is expected because increasing the PEO to polymer ratio leads to smaller particle size (Fig. 2c) and increased void space (Fig. 2d), primarily via minimizing surface tension during phase separation. According to the literature, higher molecular weight porogens require lower critical concentrations for micropore formation within the GelMA phase, but also hinder proper crosslinking of the continuous GelMA phase at lower concentrations across a range of GelMA types [19]. This may be due to the fact that higher molecular weight porogens are more prone to aggregate, which results in larger emulsion droplets due to the increased hydrophobicity of polymer chains and a larger hydrodynamic radius, which enhances phase separation. In addition, PEO may affect the crosslinking between GelMA colloidal gels, especially due to the molecular weight of PEO. Here, PEO was selected at 300,000 g/mol and was used for the fabrication of the colloidal hydrogels, which were then washed multiple times with PBS to minimize the PEO effect. Once colloids have formed, the gelatin/GelMA gel possesses reversible sol–gel behavior that helps maintain its solid form without chemical crosslinking and retains PEO at low temperatures. Thus, we included a washing process to minimize the PEO effect on the crosslinking of colloids to yield stable colloidal hydrogels. One distinction between varying the polymer:PEO ratio and the GelMA/gelatin ratio lies in how the Young's modulus changes at different ratios (Fig. 2e). When the polymer:PEO ratio was altered in either direction, the Young's modulus increased. Interestingly, a 4:1 ratio of polymer to PEO showed the highest Young's modulus; however, the absolute increase remained within a range of roughly 1 kPa. The leaching of gelatin alongside PEO resulted in no significant differences between groups with respect to hydrolytic degradation (Fig. 2f). In contrast, we observed a large reduction in mass with an increased proportion of PEO compared with the 4:1 ratio. In the presence of enzymatic solutions using collagenase type IV, the 4:1 sample exhibited a greater enzymatic degradation rate than other samples, primarily due to the fact that it included a larger portion of crosslinked polymer, which is subject to degradation, even though the overall gel particle size was larger than the others. In contrast, the 1:1–1:4 samples exhibited similar levels of resistance to enzymatic

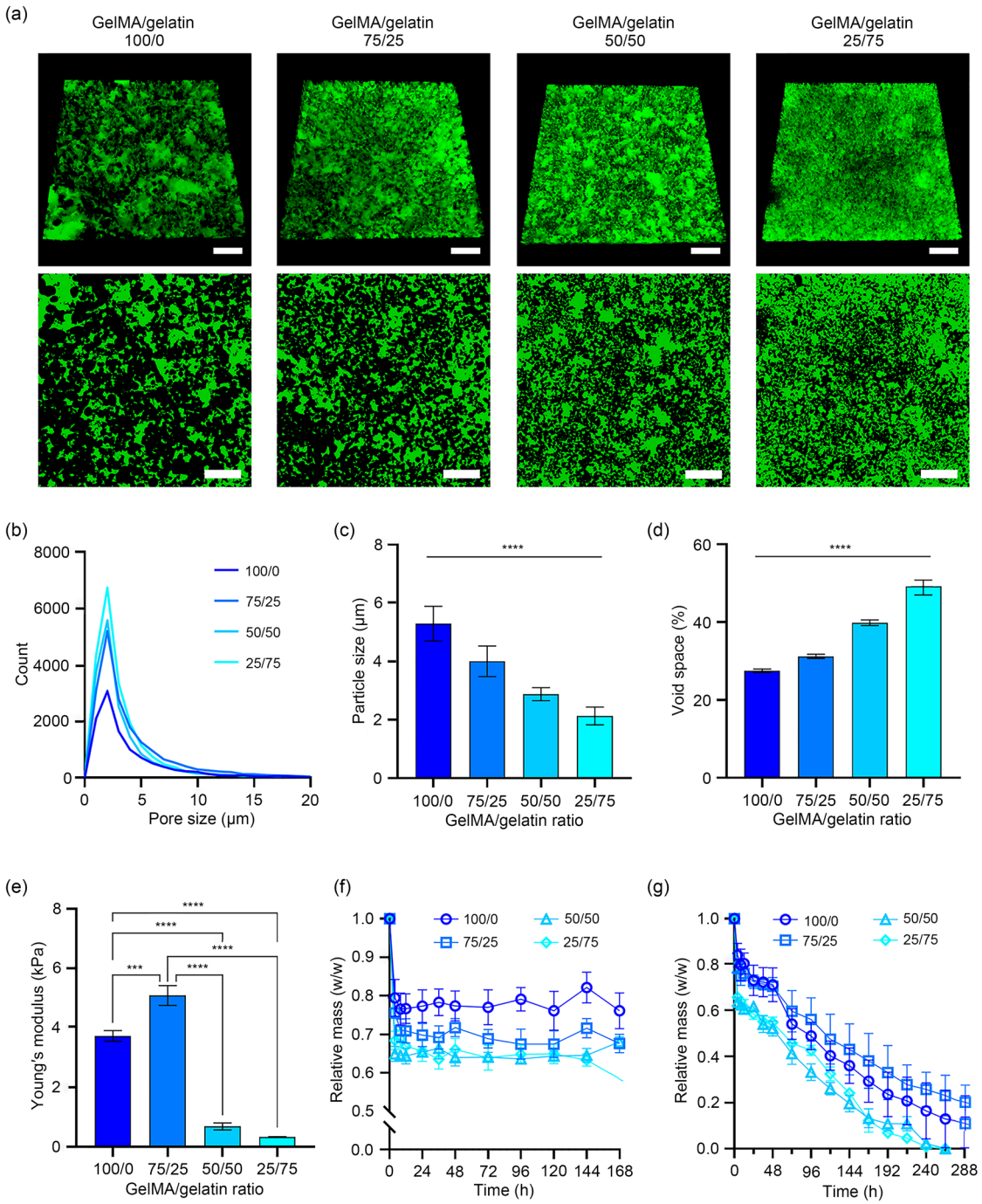

Fig. 1 Characterization of colloidal gels with various GelMA:gelatin ratios. **a** Confocal fluorescent micrographs of colloidal gels composed of GelMA and gelatin with different ratios. Images show the results of an FITC-dextran infiltration test (top row: *z*-stacked images; bottom row: a representative surface of colloidal gels observed using a confocal microscope). Scale bar: 50 μm. **b** Pore size distribution of colloidal hydrogel particles after crosslinking. Results are calculated from fluorescent micrograph images (i.e., 30 slices of one gel sourced from fluorescent micrograph images). **c** Particle size of colloidal hydrogels after crosslinking as calculated from fluorescent micrographs. **d** Void space of colloidal hydrogels composed of different GelMA and gelatin ratios calculated using fluorescent micrographs. **e** Young's modulus of different GelMA and gelatin ratios. **f** Hydrolytic degradation in PBS and **g** enzymatic degradation rate of hydrogels over time in a type IV collagenase solution. Data are expressed as mean±standard deviation (n=3). $^{***}p$<0.001, $^{****}p$<0.0001. GelMA: gelatin methacryloyl; FITC: fluorescein isothiocyanate; PBS: phosphate-buffered saline; w/w: weight-to-weight

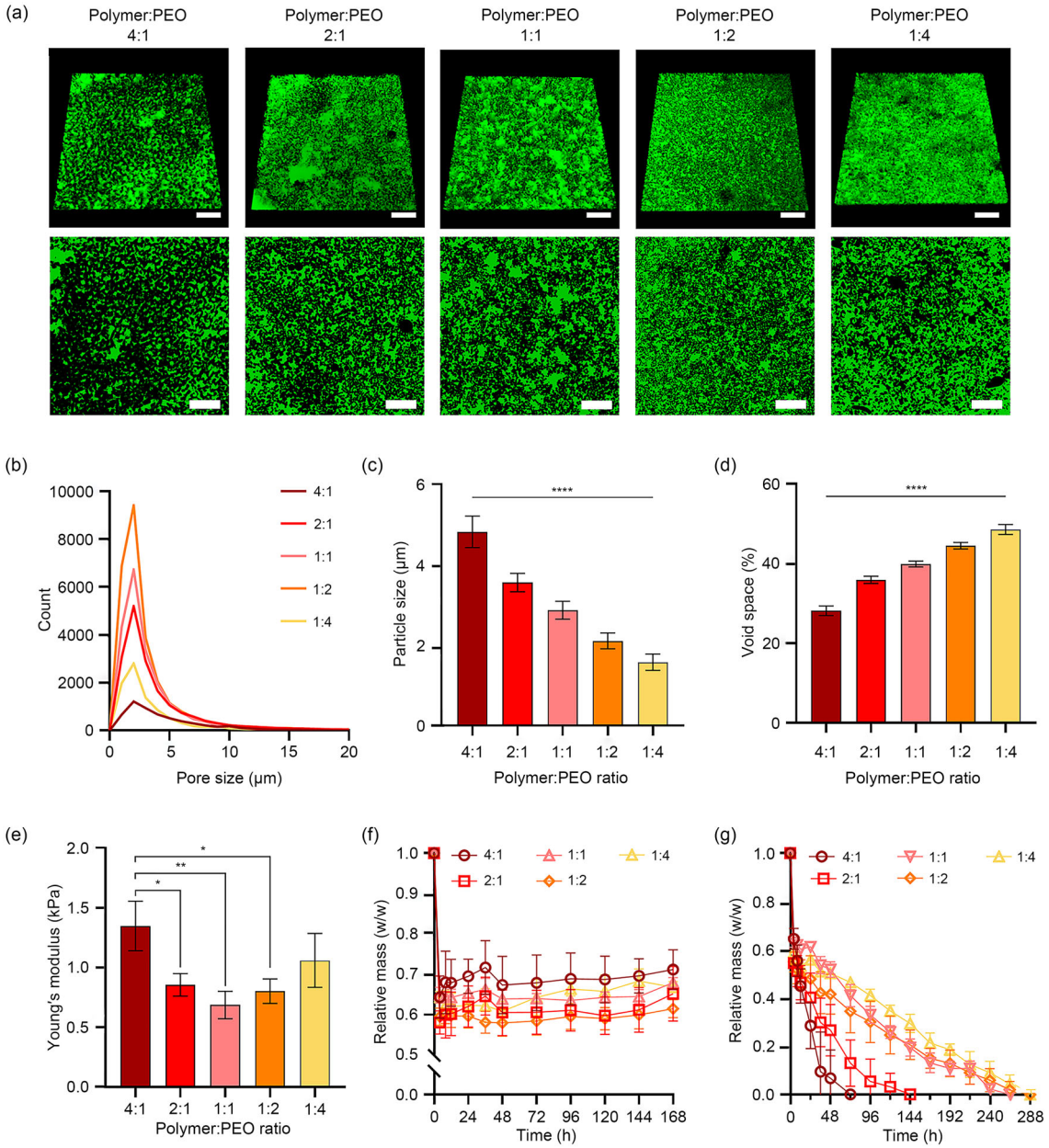

Fig. 2 Characterization of colloidal gels at different polymer (mixture of gelatin and GelMA) to PEO ratios. **a** Confocal fluorescent micrographs of colloidal hydrogels with different ratios of polymer (mixture of gelatin and GelMA) to PEO visualized using FITC-dextran infiltration tests (scale bar: 50 μm). **b** Pore size distribution, **c** hydrogel particle size, and **d** void space of colloidal hydrogels with different ratios of polymer (mixture of gelatin and GelMA) to PEO as determined using fluorescent micrograph images (i.e., 30 slices of one gel sourced from fluorescent micrograph images). **e** Young's modulus determination of colloidal hydrogels containing different ratios of polymer (mixture of gelatin and GelMA) to PEO. Also shown are **f** hydrolytic degradation in PBS and **g** enzymatic degradation rate of novel hydrogels over time in a 1.5 μg/mL collagenase type IV solution. Data are expressed as mean±standard deviation (n=3). $^{*}p<0.05$, $^{**}p<0.01$, $^{****}p<0.0001$. GelMA: gelatin methacryloyl; PEO: poly(ethylene oxide); FITC: fluorescein isothiocyanate; PBS: phosphate-buffered saline; w/w: weight-to-weight

degradation (Fig. 2g). Both here and elsewhere, adjustment of the physical and mechanical characteristics of colloidal gels has been convincingly demonstrated via modulation of polymer material ratios. Here, we selected a 50/50 ratio of GelMA to gelatin and a 1:1 polymer to PEO ratio for the construction of composite systems incorporating OMP. The inherent porous structure of colloidal hydrogels led to further exploration of their tunability, focusing on visualizing this porous nature across different compositions. Initially, we examined the distinctions between a colloidal hydrogel (i.e., with a 50/50 weight ratio) and bulk GelMA (0.075 g/mL) (Fig. S3 in Supplementary Information). In addition to an initial phase of gelatin leaching, which was also a noticeable influence on the volume-to-volume ratio, colloidal and bulk hydrogels exhibited similar weight-to-weight hydrolytic stability. While bulk GelMA hydrogel demonstrates a greater Young's modulus compared to a colloidal hydrogel, we hypothesized that tunability could be further exploited to bridge this gap for colloidal hydrogel. The porous structure of the colloidal hydrogel resulted in faster oxygen saturation and a higher influx of oxygen compared to bulk GelMA. Moreover, the microstructure of the polymeric matrix the colloidal hydrogel carrying OMPs, possessed a larger portion of voids and interconnected microporous networks compared to bulk hydrogels. This resulted in significant differences in oxygen diffusion behavior in terms of partial pressure of oxygen over time and oxygen saturation change, as illustrated in Figs. S3e and S3f (Supplementary Information). To evaluate the importance of the partial pressure of oxygen (pO_2), both bulk and colloidal hydrogels, each with dimensions of 5 mm in diameter and 5 mm in height, were prepared and then placed in oxygen-depleted PBS inside an anoxic chamber at 25 °C. An optic sensor probe was then inserted into both gels to measure their oxygen levels as the chamber transitioned to normoxic conditions. The results showed a considerable disparity in oxygen diffusion rates. Within 60 min, the oxygen level became saturated at about 60 mmHg (1 mmHg=133 Pa) of pO_2 for the colloidal gels, whereas the bulk hydrogels took more than 120 min to reach the same partial pressure level within the gel matrix.

Development of OMPs using $nCaO_2$ and $nMnO_2$ nanoparticles

To produce OMPs, $nCaO_2$ and $nMnO_2$ were incorporated into a PCL-based microparticle. The determination of the ratio between $nMnO_2$ and $nCaO_2$ involved a delicate balance, and we aimed to optimize the properties of the final composite while ensuring compatibility with PCL encapsulation during emulsion. Various factors, such as the desired oxygen release rate, encapsulation efficiency, and propensity for aggregation, were considered during this process.

First, experiments were conducted to evaluate the dispersion of $nCaO_2$ within the PCL matrix and its impact on oxygen release kinetics. Here we aimed for a uniform dispersion to enhance composite performance. Similarly, optimizing $nMnO_2$ in PCL requires careful consideration of concentration levels, since this can prevent aggregation and ensure homogeneous distribution within the polymer matrix. Approximate calculations were employed to estimate oxygen release, and we attempted to avoid exceeding certain thresholds known to lead to aggregation or the hindering of encapsulation during emulsion. Based on prior findings [48], it was observed that exceeding specific percentages of $nMnO_2$ or $nCaO_2$ could result in aggregation or difficult encapsulation. These findings informed the determination of appropriate ratios to achieve optimal performance while mitigating potential hurdles for manufacturing processes.

When fabricating OMPs using the double emulsion method, we chose nanosized CaO_2 particles to ensure a homogeneous distribution of materials capable of generating oxygen. Further TEM analysis of $nCaO_2$ revealed its arrangement in clusters with a spherical shape (Fig. 3a and Fig. S4 in Supplementary Information). Subsequently, elemental mapping (EDS) revealed calcium and oxygen elements, thereby confirming the successful synthesis of nanosized CaO_2 like previous work [48]. The size distribution of $nCaO_2$ is presented in Fig. 3b and shows an average size around (623.4±111) nm; in addition, we observed its rough surface and spherical shape via SEM (Fig. S4a in Supplementary Information). Next, TEM images of $nMnO_2$ demonstrated the formation of 2D metal oxide structures that resemble graphene-like sheets (Fig. 3c and Fig. S4 in Supplementary Information), with Mn and O element detection (Fig. 3d). Compared to OMP containing only $nCaO_2$, as shown in Fig. S5a (Supplementary Information), OMP containing both $nCaO_2$ and $nMnO_2$ shows a rough surface, showing that some of both nanoparticles adhere to the surface of OMPs (Fig. 3e), and that the OMPs were approximately 1 μm in diameter (Fig. 3h), which is similar to the size in our previous studies [46]. Overall, OMP-laden colloidal hydrogels maintained microporous structures with a pore size of (7.35 ± 2.77) μm (Fig. 3f) and probably included both spherical colloidal hydrogels and voids generated by the presence of PEO and gelatin. Importantly, the OMPs were well embedded within the colloidal hydrogel matrix (Fig. 3g). Finally, a higher concentration of OMPs (i.e., 0.5% OMP-Gel) resulted in a greater distribution of OMPs within the porous hydrogel network (Figs. S5b and S5c in Supplementary Information).

Development of OMP-laden colloidal bioinks and assessment of their oxygen-releasing behavior

Next, OMPs were effectively incorporated into the printing process by mixing them with colloidal solutions at a

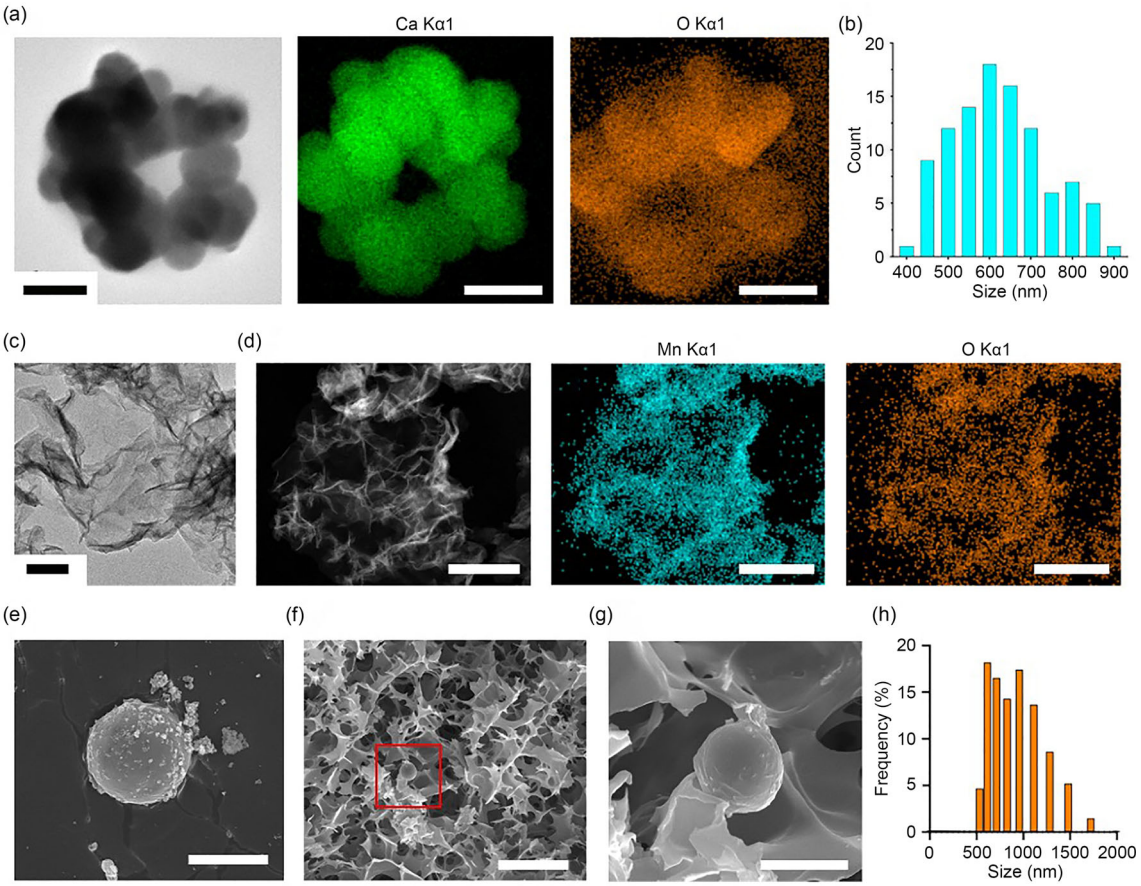

Fig. 3 Characterization of OMPs, including $nCaO_2$ and $nMnO_2$ nanoparticles. **a** TEM and EDS mapping images of $nCaO_2$ (scale bar: 1 μm). **b** Size distribution of $nCaO_2$ calculated using SEM images. **c** TEM morphology of $nMnO_2$ (scale bar: 100 nm). **d** TEM and EDS mapping images of $nMnO_2$ (scale bar: 250 nm). **e** SEM image of OMPs composed of $nCaO_2$ and $nMnO_2$ encapsulated in PCL microspheres (scale bar: 5 μm). **f** SEM image of a cross-sectional view of 0.1% OMP-laden colloidal gel (scale bar: 20 μm), and **g** high-magnitude image (scale bar: 5 μm). **h** Size distribution of OMPs was analyzed by Zetasizer. OMPs: oxygen-generating microparticles; TEM: transmission electron microscopy; EDS: energy-dispersive X-ray spectroscopy; SEM: scanning electron microscope; PCL: polycaprolactone

concentration of 0.5% relative to the total bioink volume. Microscopic examination of UV crosslinking showed that OMP was uniformly dispersed within the colloidal hydrogel matrix, thus demonstrating its homogeneity (Fig. 4a). Next, before mixing OMP with colloidal hydrogels, OMPs were first coated with high DoM of GelMA to prevent aggregation across a range of concentrations. In a previous study, GelMA coating of the surface of hydrophobic OMPs was performed using GelMA as a bio-surfactant, and this was found to effectively disperse hydrophobic nanoparticles such as carbon nanotubes and graphene [58]. Next, to visualize each component in engineered oxygen-containing bioinks, we used FITC-conjugated GelMA for colloidal hydrogels and rhodamine-conjugated PCL for the recognition of OMPs in colloidal hydrogels (Fig. 4b). Regardless of OMP concentration, we found that colloidal hydrogels were compactly distributed (i.e., (2.98±1.87) μm). This may be due to the fact that the methodology for creating OMP-Gel includes the prior fabrication of a colloidal gel and the separate synthesis of OMPs. These components were subsequently mixed before undergoing crosslinking. Analysis of the absolute relative mass loss ratios indicated both hydrolytic degradation (Fig. 4c) and enzymatic degradation (Fig. 4d) but showed no significant differences between the groups containing 0.0%–0.5% of OMP-incorporated composite hydrogels.

Next, a colloidal gel consisting of FITC-conjugated gelatin and GelMA (ratio: 50:50) was examined using confocal microscopy to assess void formation resulting from gelatin dissolution. As illustrated in Fig. 4e, the presence of FITC-conjugated gelatin allowed for the clear observation of densely packed colloidal structures with diameters of a few microns during colloidal gel preparation. Moreover, after 24 h of incubation in PBS at 37 °C, we observed a notable decrease in the fluorescence signal, indicating significant dissolution of gelatin colloids and thereby creating

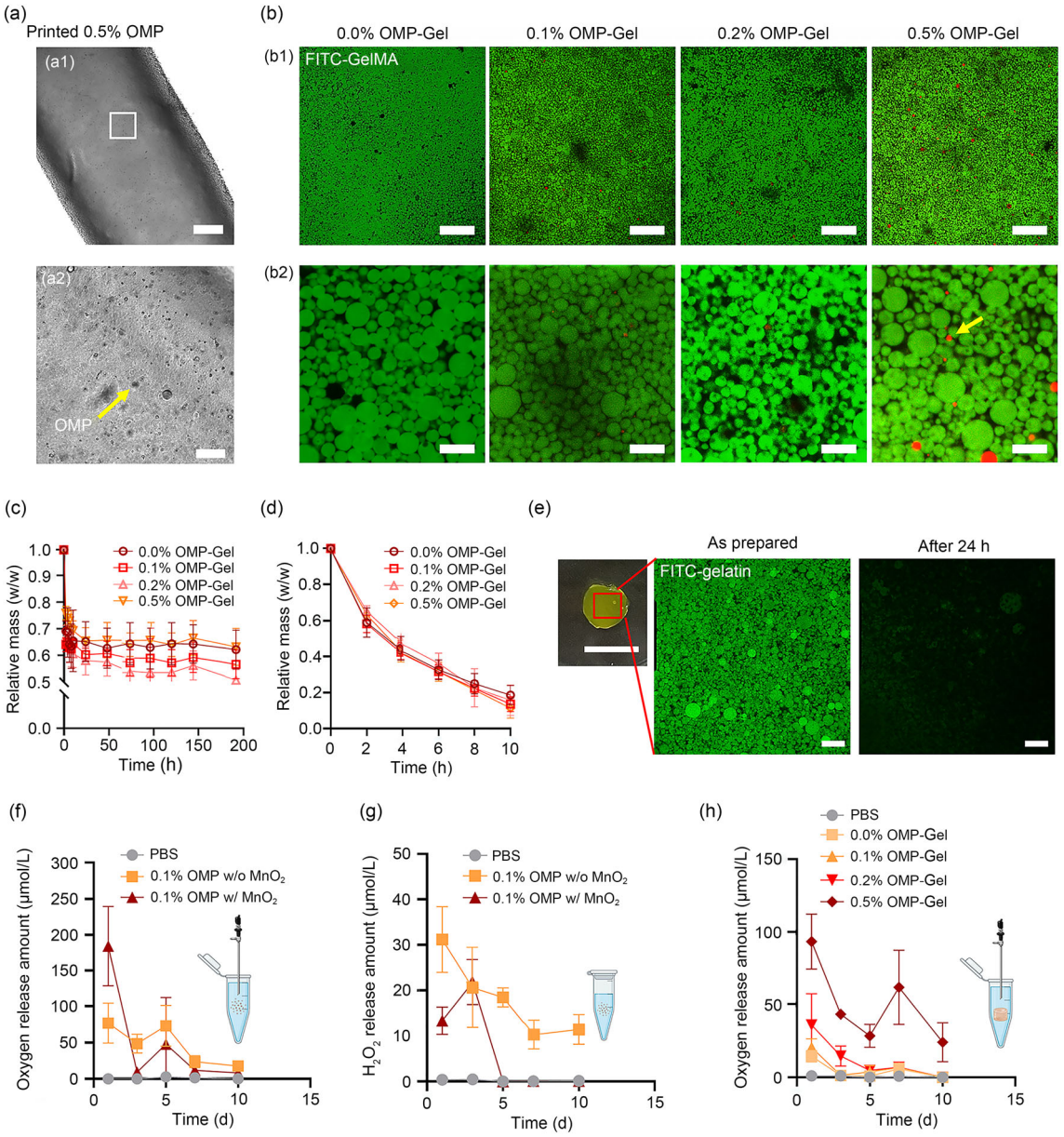

Fig. 4 Surface morphologies of OMP-laden colloidal bioinks and characterization of the post-crosslinking hydrolytic stability, enzymatic stability, and oxygen release behavior of OMP-Gels. **a** (a1) Bright-field image of printed OMP-Gel fibers containing 0.5% OMP (scale bar: 500 μm) and (a2) higher magnitude micrograph of OMP-Gel (scale bar: 100 μm). **b** Confocal images of OMP-Gel composed of FITC-conjugated GelMA (scale bar: 50 μm (b1) and 10 μm (b2)) with different concentrations of OMPs. Here the yellow arrow indicates OMP made of rhodamine-conjugated PCL. **c** Relative mass loss ratio of OMP-Gels upon following hydrolytic degradation in PBS (n=3) at 37 °C. **d** Relative mass loss ratio of OMP-Gels upon following enzymatic degradation in 1.5 μg/mL type IV collagenase solution at 37 °C (n=3). **e** Photograph and confocal image of a colloidal gel composed of FITC-conjugated gelatin (scale bar: 1 cm). Also shown is a confocal image of a colloidal gel composed of FITC-conjugated gelatin after 24-h incubation in PBS at 37 °C (scale bar: 20 μm). **f** Oxygen release profiles of OMPs with and without $nMnO_2$ following incubation in PBS for 10 d at 25 °C (n=3). **g** H_2O_2 release profiles of OMPs with and without $nMnO_2$ following incubation in PBS for 10 d at 25 °C (n=3). **h** OMP-Gels with various concentrations of OMPs following incubation in PBS for 10 d at 37 °C (n=3). Data are expressed as mean±standard deviation. OMP: oxygen-generating microparticle; FITC: fluorescein isothiocyanate; GelMA: gelatin methacryloyl; PBS: phosphate-buffered saline; w/w: weight-to-weight; w/o: without; w/: with

additional porosity. This reduction in fluorescence signal correlates closely with an observed decrease in swelling mass ratio following the initial 3-h incubation period in PBS, which is attributed to gelatin dissolution (Fig. 4c).

Next, we assessed the oxygen release profiles of OMPs and OMP-Gels. To assess different oxygen release profiles based on the presence of $nMnO_2$ in OMPs, 0.1% concentrations of OMPs with and without $nMnO_2$ were dispersed in oxygen-depleted PBS, and then, their oxygen levels were monitored using an optic sensor probe while OMPs and OMP-Gels were present in PBS held at 25 °C for 10 d (Fig. 4f). Remarkably, even by the Day 1 time point, 0.1% OMP samples containing $nMnO_2$ released approximately 2.3 times more oxygen ((180.1±55.0) μmol/L) than samples without $nMnO_2$ ((77.4±27.7) μmol/L). This finding indicated the active role of $nMnO_2$ as a nanozyme in converting excess H_2O_2 into oxygen. This was consistent with an H_2O_2 release graph (Fig. 4g), which compares two OMP types that differ only in whether $nMnO_2$ is also present. This result confirmed that $nMnO_2$ effectively functions as a nanozyme and agrees with similar results previously reported in the scientific literature [48]. Furthermore, increasing the OMP content in the colloidal hydrogel composites from 0.0% to 0.5% resulted in significant variation in released oxygen levels, which ranged from (14.5±3.9) μmol/L to (93.5±18.8) μmol/L (Fig. 4h and Fig. S6 in Supplementary Information). Thus, we conclude that an increase in oxygen level from (14.5±3.9) μmol/L (pO_2: (8.3±2.2) mmHg) to (93.5±18.8) μmol/L (pO_2: (53.5±10.8) mmHg) occurred in response to increasing the OMP content. The OMP-Gel composition at 0.1% exhibited a modest oxygen release of around (6.7±2.9) μmol/L (pO_2: (4.2±1.8) mmHg) over seven days, thereby creating a suitable environment for mild hypoxia. Hence, it can be inferred that manipulation of the quantity of OMP present enabled the adjustment of partial oxygen levels. In particular, our data suggest that an oxygen-rich environment of approximately 1%–2% can be sustained for approximately 5–7 days using OMP concentrations between 0.1% and 0.2% in the composites. Moreover, for use cases involving the engineering of bone-like structures, OMP concentrations ranging from 0.2% to 0.5% can be selected to support extended hMSC culture durations in the printed construct. This would be sufficient to enable osteogenic differentiation and may ensure prolonged cell viability under anoxic conditions.

Printability of OMP-laden colloidal bioinks

Since granular-based microgels face deformation challenges within a bioprinting apparatus [54], understanding the distinctive rheological characteristics of OMP-laden colloidal bioinks is critical. Filamentous extrusion of bioinks with OMPs was therefore performed to permit observation of bioink stability following dispensing (Fig. 5). Here, we report the length of the hanging filaments (L_f) for each bioink (Fig. 5b). Overall, our results reveal that extruded OMP-Gel bioinks generated longer suspended filaments than a control group lacking OMPs. The hanging fibers within the OMP-Gel bioinks displayed remarkable uniformity and remained intact without breaking or detaching. In addition, a composite bioink containing 0.5% OMPs generated the longest suspended filament (i.e., about 20 mm), in contrast with the filament from the bioink without OMP, which was only about 12 mm in length (Fig. 5b).

Any material's ability to produce a filament and maintain consistent extrusion is directly associated with its shear-thinning and rapid shear recovery properties. We therefore report the viscosity properties of the OMP-Gel bioinks analyzed here (Fig. 5c). Moreover, as shown in Fig. 5d, the storage moduli either increased or remained relatively stable within the frequency range of 0.1 to 100 rad/s. In general, the incorporation of OMP improved the shear-thinning rheological properties of the colloidal hydrogel bioink. As it maintains its rheological characteristics, the viscosity value increases with OMP concentration. One hypothesis explaining the increase in stability and printability after adding OMP to the colloidal gels is that the existence of oxygen on the surfaces of $nMnO_2$ and $nCaO_2$ promotes the establishment of hydrogen bonds with gelatin molecules. In addition, as shown by the zeta potential values (Fig. 5e), strong electrostatic interactions between OMP and the colloidal hydrogel may affect printability. These results also indicate that $nMnO_2$ was incorporated not only within the PCL microsphere but also on the surface of PCL, where it affects the surface charge of the colloidal gel and the OMP mixture. This observed behavior appears to be linked to the presence of $nCaO_2$ on the surface of the particles. Furthermore, as the amount of MnO_2 increases, a larger area of $nCaO_2$ becomes exposed. Notably, if the measurements were conducted in a liquid medium, $nCaO_2$ can initiate a breakdown, causing the formation of $Ca(OH)_2$. With the gradual introduction of MnO_2, the balance of the reaction shifts, favoring the production of $Ca(OH)_2$. This leads to an elevated presence of Ca^{2+} ions on the particle surface, thereby generating increased potential zeta values. A frequency sweep test demonstrated that the OMP-Gel bioinks displayed characteristics resembling those of solid-like hydrogel materials (Fig. 5f). Furthermore, a cyclic recovery test was conducted to investigate how quickly viscosity was restored following extrusion. We found that under low strain conditions the 0.5% OMP-Gel displayed characteristics resembling a hydrogel, and that these properties could be reversed under high strain conditions, where it then displayed liquid-like behavior.

To assess the stability of OMP-laden colloidal bioinks, we conducted a quantitative analysis by evaluating the fidelity of pore shapes, as depicted in Fig. 6a. To do so, we employed

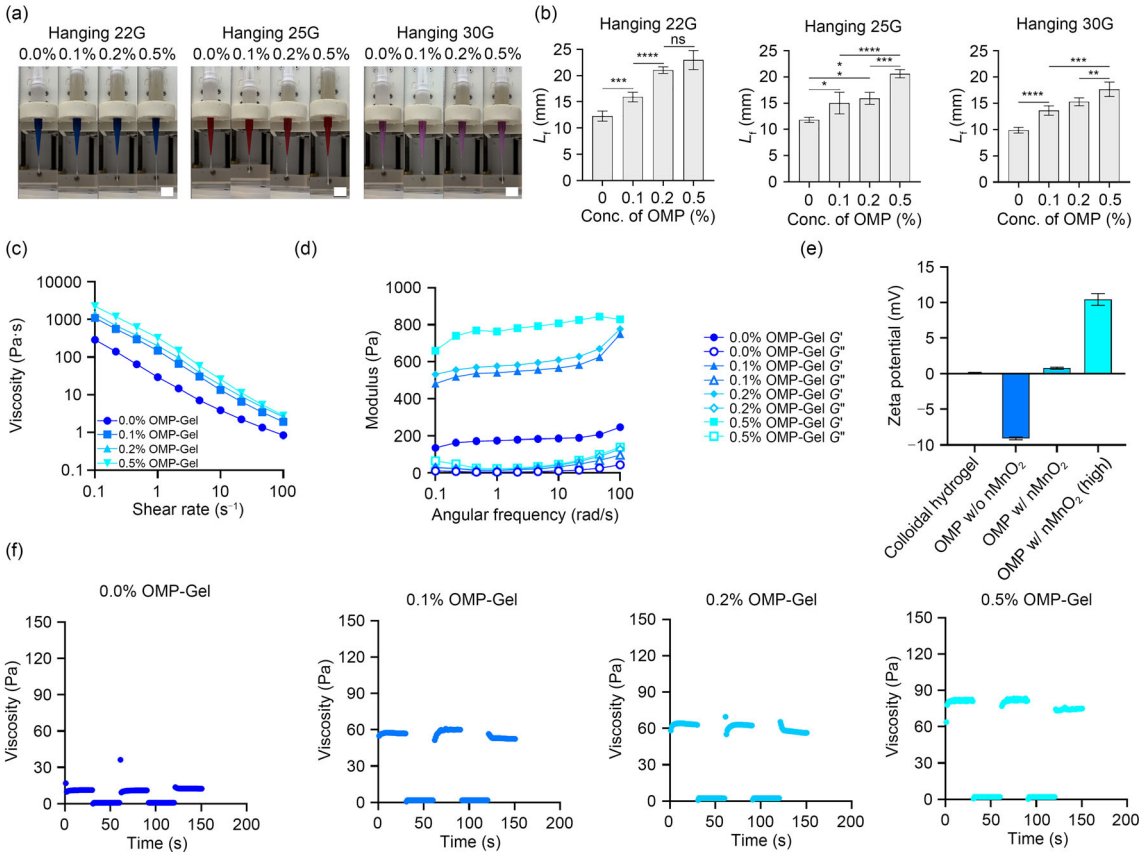

Fig. 5 Hanging fiber assessments and rheological behaviors of OMP-Gels and surface charge analysis of an OMP-laden colloidal ink. **a** Photographs of hanging filaments of OMP-Gels with various concentrations of OMPs. Assessment was performed using different needle gauges (scale bar: 1 cm). **b** Calculated lengths of hanging filaments of OMP-Gels using different needle gauges ($^{*}p<0.05$, $^{**}p<0.01$, $^{***}p<0.001$, $^{****}p<0.0001$, ns: not significant; $n=5$). **c** Viscosity of OMP-Gel bioinks with various concentrations of OMPs as a function of shear rate. **d** Storage and loss modulus of OMP-Gel bioinks with various concentrations of OMPs as a function of angular frequency. **e** Zeta potential of samples including colloidal bioinks containing various amounts of OMPs ($n=3$). **f** Viscosity recovery graph of OMP-Gel bioinks with different OMP concentrations. Data are expressed as mean±standard deviation (**b**, **e**). OMP: oxygen-generating microparticle; Conc.: concentration; w/o: without; w/: with

needles with different gauges (i.e., 22G, 25G, and 30G), each of which has a distinct inner diameter (i.e., 410, 250, and 150 μm, respectively). We then calculated their printability index (P_r) by measuring the perimeter and area of the pores (Fig. 6b and Fig. S7 in Supplementary Information). For a 1 mm×1 mm size, all printed fibers merged, indicating poor pore shape fidelity due to the small scale of the design. In general, we observed that as the needle tip size decreased, the P_r value approached 1. For colloidal bioinks without OMP, P_r values ranged from 0.88 to 0.93, suggesting a deviation at $P_r<1$, likely due to the low viscosity of the GelMA-gelatin colloidal hydrogel bioink itself. Conversely, as more OMPs were added, P_r values increased from approximately 0.95 to 0.99, indicating that OMP enhanced overall bioink viscosity and led to improved geometric accuracy (Fig. 6c). This is because the printed filament diameter is directly affected by the pressure, printing speed, and needle diameter. When maintaining constant pressure, lower printing speeds result in thicker filaments due to enhanced material deposition (Fig. 6d). Conversely, higher printing speeds cause filament stretching, which reduces their diameter and, in some cases, interrupts bioink deposition on the substrate [59]. In addition, a smaller needle diameter necessitates higher pressure for extruding an equivalent amount of bioink. With constant pressure and printing speed, the diminished cross-sectional area of the smaller needle constrained material deposition, resulting in a thinner filament (Fig. S8 in Supplementary Information).

Next, we used rhodamine-conjugated GelMA to form colloidal bioinks that can visually demonstrate the versatility of constructing different spatial shapes. We successfully created various freeform shapes that closely resembled the intended morphology of a model (Fig. 7a). Furthermore, we assessed the stacking capability of colloidal hydrogel-based bioinks

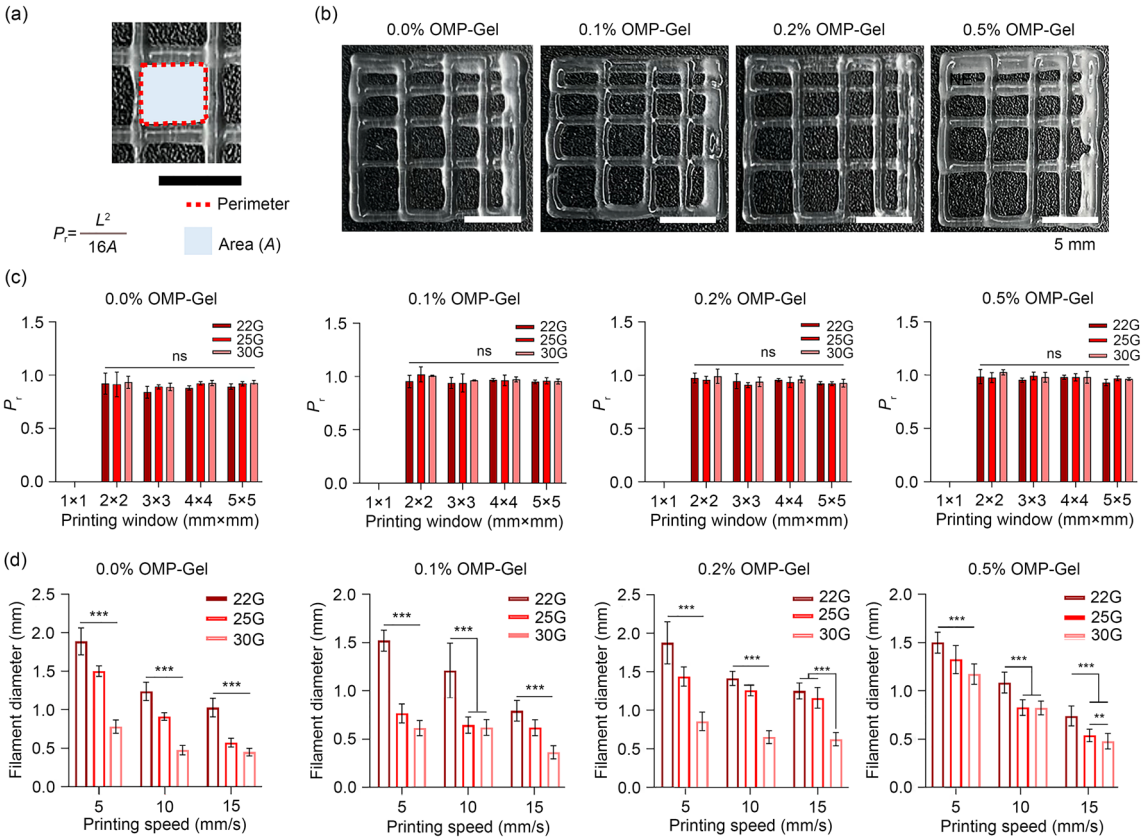

Fig. 6 Printability of OMP-laden colloidal bioinks. **a** Extrusion printability of OMP-laden colloidal bioinks based on different printability window sizes. Printability windows tested here ranged from 1×1 to 5×5 (mm×mm) (Printability index (P_r) and scale bar: 5 mm). **b** Photographs of printed patterns with different concentrations of OMP-laden colloidal bioinks using a 22G needle gauge (scale bar: 5 mm). **c** Calculated P_r of printed patterns produced using different concentrations of OMP-laden colloidal bioinks (ns: not significant; n=3). **d** Diameters of printed filaments using different concentrations of OMP-laden colloidal bioinks and different printing speeds ($^{**}p$<0.01, $^{***}p$<0.001; n=3). Data are expressed as mean±standard deviation. OMP: oxygen-generating microparticle

to emulate the intricate architecture of organs or tissues. Thus, we printed simple patch designs with different layer counts, i.e., ranging from 2 to 6 layers. As we increased the height of the printed construct, the colloidal hydrogel-based bioinks generally maintained their structural integrity well. Finally, to demonstrate the macroscopic scalability of the OMP-Gel, freeform 3D structures resembling various tissue types, including bone, heart, brain, and hair, were successfully fabricated using extrusion-based bioprinting. The printed constructs had the following expended volumes: about 0.16 mL for bone, 2.5 mL for heart, 3.4 mL for brain, and 0.1 mL for hair. Both fluorescence (Fig. 7b) and bright-field (Fig. 7c) images of the tissue-mimic constructs identified visible patterns in the printed structure, and that multiple layers were effectively stacked without collapse. These effects serve as further confirmation of the printability and stability of the novel bioink described here and verify its successful replication of desired tissue shapes.

Cytocompatibility of OMP and 3D-printed constructs created using OMP-laden colloidal bioinks containing cells

We then investigated the cytocompatibility of OMPs using HDFs. In general, both OMPs that contained only $nCaO_2$ and those that contained a combination of both $nCaO_2$ and $nMnO_2$ were associated with high levels of cell survival (Figs. 8a and 8b). These results indicated that there was no toxicity to cells cultured in media containing different OMP concentrations. Here, cell viability tests were conducted under anoxic conditions to assess the potential effects of prolonged exposure to excessive oxygen release, which can lead to oxidative stress and cell damage. Both HDFs and hMSCs were seeded onto gel surfaces with varying concentrations of OMPs (i.e., ranging from 0.0% to 0.5%) and were cultured for seven days under anoxic conditions. Notably, we observed excessive oxygen release from the 0.5% OMP-Gel, as indicated by the results of the oxygen release graph shown

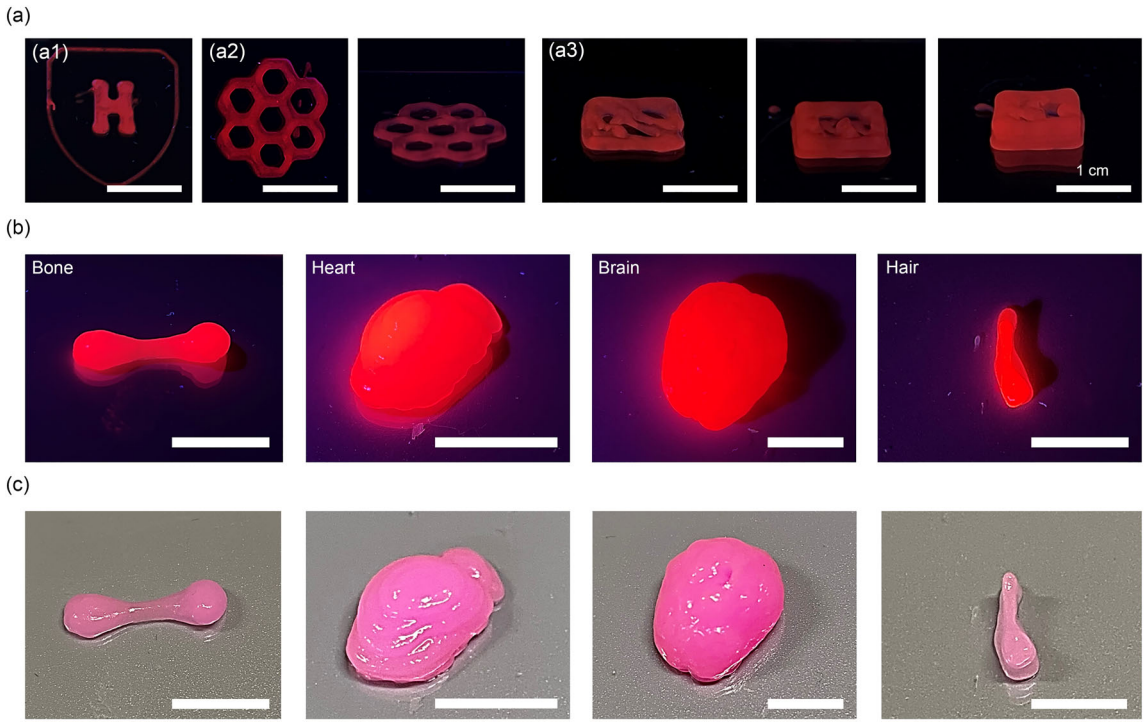

Fig. 7 3D-printed constructs using OMP-laden colloidal bioinks. **a** Photographs of various printed constructs using 0.1% OMP-Gel: (a1) a pattern motif, (a2) honeycomb (top and side views), and (a3) patch-type designs with different numbers of layers (i.e., 2, 4, and 6 layers; scale bar: 1 cm). **b** Fluorescent photographs and **c** photographs of printed tissue-mimic constructs of bone, heart, brain, and hair composed of 0.1% OMP-Gel (scale bar: 1 cm). OMP: oxygen-generating microparticle

in Fig. 4h; this was also associated with lower cell viability, particularly noticeable in HDFs, after seven days of culture (Figs. 8c and 8e). In contrast, hMSCs showed similar cell viability levels regardless of OMP concentration (Figs. 8d and 8f).

Next, we assessed cell viability within printed constructs by culturing both HDFs and hMSCs for seven days in 0% and 0.1% OMP-Gels under hypoxic conditions (i.e., with oxygen levels below 1%) (Fig. 8g and Fig. S9 in Supplementary Information). To do so, one layer of the designed tissue constructs was printed with a cell density of 5×10^6 cells/mL and was photocrosslinked using UV light. Over the seven-day culture period, most of both cell types within bioprinted constructs remained highly viable with excellent cell spreading. We conclude that cell viability was not affected by the extrusion bioprinting process, and that the suggested OMP and colloidal hydrogel formulations offered favorable microenvironments for cell adhesion and growth, were characterized by highly porous structures, and facilitated localized oxygen delivery. Moreover, to illustrate the distribution and viability of cells within a printed construct, we added a representative high-magnitude live/dead image to Fig. 8g, and provide multiple high-magnitude live/dead images captured at various locations of the printed construct in Fig. S9 (Supplementary Information). These figures show that cells were uniformly distributed across each construct and in both groups regardless of the imaging area. Furthermore, we observed a relatively high proportion of live cells than dead cells in the 0.1% OMP-Gel relative to the 0% OMP-Gel. This difference was particularly evident in the brain- and heart-shaped constructs in which volume seemed to be higher than for the other designs (Fig. 8g and Fig. S10 in Supplementary Information).

We then used PCR to assess the expression of genes related to differences in oxygen levels (e.g., HIF-1α). To do so, samples containing HDFs and hMSCs at a cell density of 2×10^6 mL^{-1} were first encapsulated and cultured under severely hypoxic conditions (i.e., <0.1% O_2). After 18 h of culturing, we observed greater differences between the 0% OMP and 0.1% OMP groups for HDFs than among the other groups (Fig. 8h). Regarding pO_2, we found that cells within the 0.1% OMP group exhibited hypoxic conditions due to the continuous release of oxygen (i.e., at levels of about 1%).

The degradation of PCL within the body is an essential consideration for the potential future use of OMPs. PCL was chosen specifically to regulate the hydrolysis rate of OMPs by minimizing their contact with water molecules; however, PCL also undergoes long-term degradation, which can take 6–12 months or longer. Moreover, H_2O_2 that released from OMPs may affect PCL oxidation, potentially accelerating

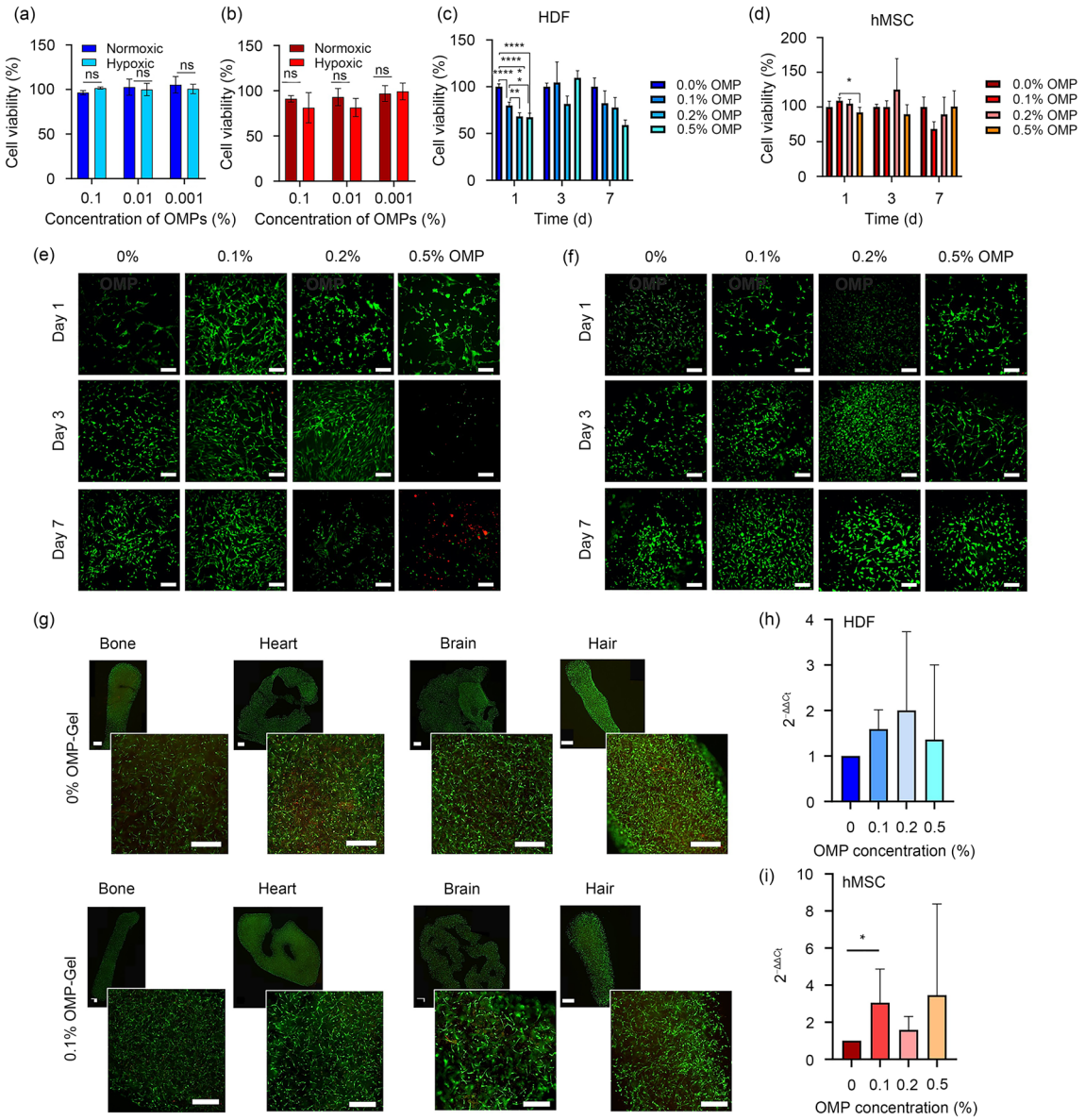

Fig. 8 Cytotoxicity of OMP and cell viability of cell-laden OMP-Gel-printed constructs. **a** Cytotoxicity of OMP including only $nCaO_2$ and **b** cytotoxicity OMP including both $nCaO_2$ and $nMnO_2$ at different OMP concentrations. Cytotoxicity was measured using HDFs in both normoxic and hypoxic conditions after one day of culture. **c** Cell viability of HDFs on the surface of OMP-Gel after seven days of culturing under anoxic (0.1% oxygen) conditions. **d** Cell viability of hMSCs on the surface of OMP-Gel after seven days of culturing under anoxic conditions (n=3). **e** Live/dead fluorescent micrographs of HDFs on the surface of OMP-Gel after seven days of culturing under anoxic conditions (scale bar: 200 μm). **f** Live/dead fluorescent micrographs of hMSCs on the surface of OMP-Gel after seven days of culturing under anoxic conditions (scale bar: 200 μm). **g** Low-magnitude live (green)/dead (red) images of 3D-printed constructs using HDF-laden 0% OMP-Gel and 0.1% OMP-Gel (scale bar for inset: 1 mm) bioinks after seven days of culturing under hypoxic (1% oxygen) conditions and a representative high-magnitude image of each construct (scale bar: 200 μm). The low-magnitude image was obtained by combining multiple images taken at several locations for entire constructs. **h**, **i** Gene expression of HIF1-α after 18 h of culturing under anoxic conditions for both **h** HDFs and **i** hMSCs. Data are expressed as mean±standard deviation (n=3). $^{*}p<0.05$, $^{**}p<0.01$, $^{****}p<0.0001$, ns: not significant. OMP: oxygen-generating microparticle; HDFs: human dermal fibroblasts; hMSCs: human mesenchymal stem cells

its degradation [60]. In addition, the degradation time of PCL-based OMPs can be easily tuned by controlling the molecular weight of PCL [61, 62]. Moreover, since H_2O_2 and the oxygen-releasing rate can both be adjusted, the relationship between the released amount of H_2O_2 and the hydrolysis of PCL can be considered further to be tailored for specific applications. Importantly, the porosity of PCL microparticles is another factor driving oxygen release before the complete degradation of PCL [62]. Here, we used $nMnO_2$ to decompose H_2O_2, which resulted in the production of Mn^{2+} and O_2. We also embedded $nMnO_2$ in PCL microparticles along with $nCaO_2$. Therefore, most of the $nMnO_2$ may be converted to Mn^{2+} and O_2 during the oxygen generation process. The metabolic pathways of Mn^{2+} are essential for various physiological functions, including protein, carbohydrate, and fat metabolism, energy regulation, connective tissue synthesis, and bone tissue mineralization [63]. However, excessive concentrations of Mn^{2+} may have harmful effects on cell viability [64–66]. Nevertheless, the potential release of Mn^{2+} arising from this system will likely be minimal, and release will occur slowly (i.e., over a few weeks). Furthermore, when considering the potential effectiveness of the metabolic pathways of $nMnO_2$ for future applications, we note that it is important to examine their behavior while embedded within biological systems.

The metabolic pathways involving $nMnO_2$ demonstrate significant variability among biological environments [63]. This is because the introduction of these nanosheets into various biological environments may trigger a diverse range of transformations and interactions. First, regarding surface interactions, we note that the structural morphology of these nanoparticles may lead to interactions with intracellular organelles such as mitochondria; this is due to the high reactivity of $nMnO_2$, which in turn stems from its 2D structure and atomically thin edge. Because of these properties, interaction with the outer mitochondrial membrane may disrupt the mitochondrial membrane potential, thereby causing mitochondrial toxicity [67]. The capacity of MnO_2 nanoparticles to generate reactive oxygen species and initiate lipid peroxidation can rectify disruptions related to antioxidants and liver enzymes, which can be responsible for cellular dysfunction and degradation [68]. Moreover, the redox activities of $nMnO_2$ allow it to engage in oxidation–reduction reactions with diverse cellular components, thereby impacting the overall cellular redox equilibrium [63]. In addition—and depending on $nMnO_2$ size and surface properties—$nMnO_2$ may be cleared from the body via processes such as phagocytosis by immune cells or by renal filtration [63]. Therefore, further determination of the potential toxicity of MnO_2 nanoparticles should involve the assessment of in vivo cytotoxicity via hematoxylin–eosin (HE) staining analysis of various tissues, including the skin, liver, spleen, lung, and stomach, after implantation of printed constructs.

Conclusions

In this study, we successfully demonstrate the incorporation of nanostructures, such as $nCaO_2$ nanoparticles and MnO_2 nanosheets, into polymeric microparticles. When integrated into viscoelastic colloidal hydrogels, this mixture enhances shear-thinning behaviors while preserving good printability performance, which is crucial for the fabrication of macroscopic constructs. We found that the use of a nanoparticle-encapsulated system was not associated with agglomeration or clogging issues, even when printing at relatively high OMP concentrations. Using a formulation including a few micron-sized spherical hydrogel particles and OMPs, we successfully used 3D bioprinting to create scaled-down conceptual representations of intricate porous human tissues (i.e., bone, heart, brain, and hair) that included oxygen-generating materials. This method shows great potential for tuning the optimal oxygen levels of bioprinted structures, which can in turn support the differentiation of specific cells into the desired tissue by offering a highly porous structure and localized oxygen delivery to neighboring cells.

Supplementary Information The online version contains supplementary material available at https://doi.org/10.1007/s42242-024-00281-7.

Acknowledgements This paper was funded by the National Institutes of Health (No. R01AR074234), AHA collaborative award (No. 944227), and the Gillian Reny Stepping Strong Center for Trauma Innovation at Brigham and Women's Hospital.

Author contributions Conceptualization was performed by SRS, SHJ, and DYA; investigation by SHJ, RDF, PVB, and JH; methodology by SHJ, PVB, JH, RDF, JHLDF, DMDS, MHK, and MLLCP; formal analysis by SHJ; supervision by SHJ, JL, and SRS; visualization by SHJ, PVB, and JH; software by SHJ, RDF, and JK; writing—original draft—by SHJ and RDF; writing—review and editing—by SHJ, PVB, JH, JL, and SRS; project administration by SRS; funding acquisition by SRS.

Declarations

Conflict of interest The authors declare that they have no conflict of interest.

Ethical approval This article does not contain any studies with human or animal subjects performed by any of the authors.

References

1. Zhang YS, Yue K, Aleman J et al (2017) 3D bioprinting for tissue and organ fabrication. Ann Biomed Eng 45(1):148–163. https://doi.org/10.1007/s10439-016-1612-8
2. Heinrich MA, Liu WJ, Jimenez A et al (2019) 3D bioprinting: from benches to translational applications. Small 15(23):1805510. https://doi.org/10.1002/smll.201805510
3. Cui X, Li J, Hartanto Y et al (2020) Advances in extrusion 3D bioprinting: a focus on multicomponent hydrogel-based

bioinks. Adv Healthc Mater 9(15):e1901648. https://doi.org/10.1002/adhm.201901648
4. Liu WJ, Zhang YS, Heinrich MA et al (2017) Rapid continuous multimaterial extrusion bioprinting. Adv Mater 29(3):1604630. https://doi.org/10.1002/adma.201770016
5. Levato R, Jungst T, Scheuring RG et al (2020) From shape to function: the next step in bioprinting. Adv Mater 32(12):e1906423. https://doi.org/10.1002/adma.201906423
6. Drury JL, Mooney DJ (2003) Hydrogels for tissue engineering: scaffold design variables and applications. Biomaterials 24(24):4337–4351. https://doi.org/10.1016/S0142-9612(03)00340-5
7. Mota C, Camarero-Espinosa S, Baker MB et al (2020) Bioprinting: from tissue and organ development to in vitro models. Chem Rev 120(19):10547–10607. https://doi.org/10.1021/acs.chemrev.9b00789
8. Chaudhuri O, Gu L, Klumpers D et al (2016) Hydrogels with tunable stress relaxation regulate stem cell fate and activity. Nat Mater 15(3):326–334. https://doi.org/10.1038/nmat4489
9. Colosi C, Shin SR, Manoharan V et al (2016) Microfluidic bioprinting of heterogeneous 3D tissue constructs using low-viscosity bioink. Adv Mater 28(4):677–684. https://doi.org/10.1002/adma.201503310
10. Ouyang LL, Armstrong JPK, Lin YY et al (2020) Expanding and optimizing 3D bioprinting capabilities using complementary network bioinks. Sci Adv 6(38):eabc5529. https://doi.org/10.1126/sciadv.abc5529
11. Hirsch M, Charlet A, Amstad E (2021) 3D printing of strong and tough double network granular hydrogels. Adv Funct Mater 31(5):2005929. https://doi.org/10.1002/adfm.202005929
12. Armstrong JPK, Burke M, Carter BM et al (2016) 3D bioprinting using a templated porous bioink. Adv Healthc Mater 5(14):1724–1730. https://doi.org/10.1002/adhm.201600022
13. Seymour AJ, Shin S, Heilshorn SC (2021) 3D printing of microgel scaffolds with tunable void fraction to promote cell infiltration. Adv Healthc Mater 10(18):e2100644. https://doi.org/10.1002/adhm.202100644
14. Daly AC, Riley L, Segura T et al (2020) Hydrogel microparticles for biomedical applications. Nat Rev Mater 5(1):20–43. https://doi.org/10.1038/s41578-019-0148-6
15. Highley CB, Song KH, Daly AC et al (2019) Jammed microgel inks for 3D printing applications. Adv Sci 6(1):1801076. https://doi.org/10.1002/advs.201801076
16. Xin SJ, Deo KA, Dai J et al (2021) Generalizing hydrogel microparticles into a new class of bioinks for extrusion bioprinting. Sci Adv 7(42):eabk3087. https://doi.org/10.1126/sciadv.abk3087
17. Shao L, Gao Q, Xie CQ et al (2020) Sacrificial microgel-laden bioink-enabled 3D bioprinting of mesoscale pore networks. Bio-Des Manuf 3(1):30–39. https://doi.org/10.1007/s42242-020-00062-y
18. Ying GL, Jiang N, Maharjan S et al (2018) Aqueous two-phase emulsion bioink-enabled 3D bioprinting of porous hydrogels. Adv Mater 30(50):e1805460. https://doi.org/10.1002/adma.201805460
19. Yi SL, Liu Q, Luo ZY et al (2022) Micropore-forming gelatin methacryloyl (GelMA) bioink toolbox 2.0: designable tunability and adaptability for 3D bioprinting applications. Small 18(25):e2106357. https://doi.org/10.1002/smll.202106357
20. Ying GL, Jiang N, Parra-Cantu C et al (2020) Bioprinted injectable hierarchically porous gelatin methacryloyl hydrogel constructs with shape-memory properties. Adv Funct Mater 30(46):2003740. https://doi.org/10.1002/adfm.202003740
21. Chen FP, Li XF, Yu YF et al (2023) Phase-separation facilitated one-step fabrication of multiscale heterogeneous two-aqueous-phase gel. Nat Commun 14(1):2793. https://doi.org/10.1038/s41467-023-38394-9
22. Murphy SV, De Coppi P, Atala A (2020) Opportunities and challenges of translational 3D bioprinting. Nat Biomed Eng 4(4):370–380. https://doi.org/10.1038/s41551-019-0471-7
23. Loessner D, Meinert C, Kaemmerer E et al (2016) Functionalization, preparation and use of cell-laden gelatin methacryloyl-based hydrogels as modular tissue culture platforms. Nat Protoc 11(4):727–746. https://doi.org/10.1038/nprot.2016.037
24. Hull SM, Brunel LG, Heilshorn SC (2022) 3D bioprinting of cell-laden hydrogels for improved biological functionality. Adv Mater 34(2):e2103691. https://doi.org/10.1002/adma.202103691
25. Michiels C (2004) Physiological and pathological responses to hypoxia. Am J Pathol 164(6):1875–1882. https://doi.org/10.1016/S0002-9440(10)63747-9
26. Huo MF, Wang LY, Chen Y et al (2020) Oxygen pathology and oxygen-functional materials for therapeutics. Matter 2(5):1115–1147. https://doi.org/10.1016/j.matt.2020.02.013
27. Willemen NGA, Hassan S, Gurian M et al (2021) Oxygen-releasing biomaterials: current challenges and future applications. Trends Biotechnol 39(11):1144–1159. https://doi.org/10.1016/j.tibtech.2021.01.007
28. Ashammakhi N, Darabi MA, Kehr NS et al (2020) Advances in controlled oxygen generating biomaterials for tissue engineering and regenerative therapy. Biomacromol 21(1):56–72. https://doi.org/10.1021/acs.biomac.9b00546
29. Gholipourmalekabadi M, Zhao S, Harrison BS et al (2016) Oxygen-generating biomaterials: a new, viable paradigm for tissue engineering? Trends Biotechnol 34(12):1010–1021. https://doi.org/10.1016/j.tibtech.2016.05.012
30. Hsieh TE, Lin SJ, Chen LC et al (2020) Optimizing an injectable composite oxygen-generating system for relieving tissue hypoxia. Front Bioeng Biotechnol 8:511. https://doi.org/10.3389/fbioe.2020.00511
31. Lu Z, Jiang X, Chen MQ et al (2019) An oxygen-releasing device to improve the survival of mesenchymal stem cells in tissue engineering. Biofabrication 11(4):045012. https://doi.org/10.1088/1758-5090/ab332a
32. Erdem A, Darabi MA, Nasiri R et al (2020) 3D bioprinting of oxygenated cell-laden gelatin methacryloyl constructs. Adv Healthc Mater 9(15):e1901794. https://doi.org/10.1002/adhm.201901794
33. Suvarnapathaki S, Wu XC, Zhang TF et al (2022) Oxygen generating scaffolds regenerate critical size bone defects. Bioact Mater 13:64–81. https://doi.org/10.1016/j.bioactmat.2021.11.002
34. Farzin A, Hassan S, Teixeira LSM et al (2021) Self-oxygenation of tissues orchestrates full-thickness vascularization of living implants. Adv Funct Mater 31(42):2100850. https://doi.org/10.1002/adfm.202100850
35. Farris AL, Lambrechts D, Zhou YX et al (2022) 3D-printed oxygen-releasing scaffolds improve bone regeneration in mice. Biomaterials 280:121318. https://doi.org/10.1016/j.biomaterials.2021.121318
36. Khorshidi S, Karimi-Soflou R, Karkhaneh A (2021) A hydrogel/particle composite with a gradient of oxygen releasing microparticle for concurrent osteogenic and chondrogenic differentiation in a single scaffold. Colloid Surf B Biointerfaces 207:112007. https://doi.org/10.1016/j.colsurfb.2021.112007
37. Shiekh PA, Mohammed SA, Gupta S et al (2022) Oxygen releasing and antioxidant breathing cardiac patch delivering exosomes promotes heart repair after myocardial infarction. Chem Eng J 428:132490. https://doi.org/10.1016/j.cej.2021.132490
38. Chen HH, Cheng YH, Tian JR et al (2020) Dissolved oxygen from microalgae-gel patch promotes chronic wound healing in diabetes. Sci Adv 6(20):eaba4311. https://doi.org/10.1126/sciadv.aba4311
39. Suvarnapathaki S, Wu XC, Lantigua D et al (2019) Breathing life into engineered tissues using oxygen-releasing biomaterials. NPG Asia Mater 11(1):65. https://doi.org/10.1038/s41427-019-0166-2

40. Guan Y, Niu H, Liu ZT et al (2021) Sustained oxygenation accelerates diabetic wound healing by promoting epithelialization and angiogenesis and decreasing inflammation. Sci Adv 7(35):0153. https://doi.org/10.1126/sciadv.abj0153
41. Gomes FL, Jeong SH, Shin SR et al (2024) Engineering synthetic erythrocytes as next-generation blood substitutes. Adv Funct Mater (Early Access). https://doi.org/10.1002/adfm.202315879
42. Gao C, Lin ZH, Wang DL et al (2019) Red blood cell-mimicking micromotor for active photodynamic cancer therapy. ACS Appl Mater Interface 11(26):23392–23400. https://doi.org/10.1021/acsami.9b07979
43. Gao M, Liang C, Song XJ et al (2017) Erythrocyte-membrane-enveloped perfluorocarbon as nanoscale artificial red blood cells to relieve tumor hypoxia and enhance cancer radiotherapy. Adv Mater 29(35):1701429. https://doi.org/10.1002/adma.201701429
44. Maharjan S, Alva J, Cámara C et al (2021) Symbiotic photosynthetic oxygenation within 3D-bioprinted vascularized tissues. Matter 4(1):217–240. https://doi.org/10.1016/j.matt.2020.10.022
45. Sheng YJ, Nesbitt H, Callan B et al (2017) Oxygen generating nanoparticles for improved photodynamic therapy of hypoxic tumours. J Contr Rel 264:333–340. https://doi.org/10.1016/j.jconrel.2017.09.004
46. Willemen NGA, Hassan S, Gurian M et al (2022) Enzyme-mediated alleviation of peroxide toxicity in self-oxygenating biomaterials. Adv Healthc Mater 11(13):2102697. https://doi.org/10.1002/adhm.202102697
47. Chen Q, Feng LZ, Liu JJ et al (2016) Intelligent albumin–MnO_2 nanoparticles as pH-/H_2O_2-responsive dissociable nanocarriers to modulate tumor hypoxia for effective combination therapy. Adv Mater 28(33):7129–7136. https://doi.org/10.1002/adma.201601902
48. dos Santos DM, Dias LM, Surur AK et al (2022) Electrospun composite bead-on-string nanofibers containing CaO_2 nanoparticles and MnO_2 nanosheets as oxygen-release systems for biomedical applications. ACS Appl Nano Mater 5(10):14425–14436. https://doi.org/10.1021/acsanm.2c02774
49. Nichol JW, Koshy ST, Bae H et al (2010) Cell-laden microengineered gelatin methacrylate hydrogels. Biomaterials 31(21):5536–5544. https://doi.org/10.1016/j.biomaterials.2010.03.064
50. Sinha AK, Pradhan M, Pal T (2013) Morphological evolution of two-dimensional MnO_2 nanosheets and their shape transformation to one-dimensional ultralong MnO_2 nanowires for robust catalytic activity. J Phys Chem C 117(45):23976–23986. https://doi.org/10.1021/jp403527p
51. Zhu YH, Wang JL, Zhang HB et al (2019) Incorporation of a rhodamine B conjugated polymer for nanoparticle trafficking both in vitro and in vivo. Biomater Sci 7(5):1933–1939. https://doi.org/10.1039/c9bm00032a
52. Cho HH, Choi JH, Been SY et al (2020) Development of fluorescein isothiocyanate conjugated gellan gum for application of bioimaging for biomedical application. Int J Biol Macromol 164:2804–2812. https://doi.org/10.1016/j.ijbiomac.2020.08.146
53. Ou Y, Cao SX, Zhang Y et al (2023) Bioprinting microporous functional living materials from protein-based core-shell microgels. Nat Commun 14(1):322. https://doi.org/10.1038/s41467-022-35140-5
54. Tuftee C, Alsberg E, Ozbolat IT et al (2023) Emerging granular hydrogel bioinks to improve biological function in bioprinted constructs. Trends Biotechnol 42(3):339–352. https://doi.org/10.1016/j.tibtech.2023.09.007
55. Daly AC (2023) Granular hydrogels in biofabrication: recent advances and future perspectives. Adv Healthc Mater (Early Access). https://doi.org/10.1002/adhm.202301388
56. Yanagisawa M, Yamashita Y, Mukai SA et al (2014) Phase separation in binary polymer solution: gelatin/poly(ethylene glycol) system. J Mol Liq 200:2–6. https://doi.org/10.1016/j.molliq.2013.12.035
57. Yamashita Y, Yanagisawa M, Tokita M (2014) Sol–gel transition and phase separation in ternary system of gelatin-water–poly(ethylene glycol) oligomer. J Mol Liq 200:47–51. https://doi.org/10.1016/j.molliq.2014.03.016
58. Hassan S, Wang T, Shi K et al (2023) Self-oxygenation of engineered living tissues orchestrates osteogenic commitment of mesenchymal stem cells. Biomaterials 300:122179. https://doi.org/10.1016/j.biomaterials.2023.122179
59. Naghieh S, Chen XB (2021) Printability–a key issue in extrusion-based bioprinting. J Pharm Anal 11(5):564–579. https://doi.org/10.1016/j.jpha.2021.02.001
60. Hsu PH, Arboleda C, Stubelius A et al (2020) Highly responsive and rapid hydrogen peroxide-triggered degradation of polycaprolactone nanoparticles. Biomater Sci 8(9):2394–2397. https://doi.org/10.1039/c9bm02019e
61. Lykins WR, Bernards DA, Schlesinger EB et al (2022) Tuning polycaprolactone degradation for long acting implantables. Polymer 262:125473. https://doi.org/10.1016/j.polymer.2022.125473
62. Bartnikowski M, Dargaville TR, Ivanovski S et al (2019) Degradation mechanisms of polycaprolactone in the context of chemistry, geometry and environment. Progr Polym Sci 96:1–20. https://doi.org/10.1016/j.progpolymsci.2019.05.004
63. Avila DS, Puntel RL, Aschner M (2013) Manganese in health and disease. Met Ions Life Sci 13:199–227. https://doi.org/10.1007/978-94-007-7500-8_7
64. Zakharcheva KA, Gening LV, Kazachenko KY et al (2017) Cells resistant to toxic concentrations of manganese have increased ability to repair DNA. Biochem Moscow 82(1):38–45. https://doi.org/10.1134/S0006297917010047
65. Chen J, Meng HM, Tian Y et al (2019) Recent advances in functionalized MnO_2 nanosheets for biosensing and biomedicine applications. Nanoscale Horiz 4(2):321–338. https://doi.org/10.1039/c8nh00274f
66. Gray EP, Browning CL, Vaslet CA et al (2020) Chemical and colloidal dynamics of MnO_2 nanosheets in biological media relevant for nanosafety assessment. Small 16(21):e2000303. https://doi.org/10.1002/smll.202000303
67. Browning CL, Green A, Gray EP et al (2021) Manganese dioxide nanosheets induce mitochondrial toxicity in fish gill epithelial cells. Nanotoxicology 15(3):400–417. https://doi.org/10.1080/17435390.2021.1874562
68. Mousavi Z, Hassanpourezatti M, Najafizadeh P et al (2016) Effects of subcutaneous injection MnO_2 micro- and nanoparticles on blood glucose level and lipid profile in rat. Iran J Med Sci 41(6):518–524